

Axial longitudinal flow in volcanic materials of the Late Carboniferous-Permian Cadí basin (Southern Pyrenees) determined from anisotropy of magnetic susceptibility

Ana Simón-Muzás^{a,*}, Antonio M. Casas-Sainz^a, Ruth Soto^b, Josep Gisbert^a, Teresa Román-Berdiel^a, Belén Oliva-Urcia^c, Emilio L. Pueyo^b, Elisabet Beamud^d

^a Departamento de Ciencias de la Tierra, Geotransfer-IUCA, Universidad de Zaragoza, 50009 Zaragoza, Spain

^b IGME, Instituto Geológico y Minero de España, Unidad de Zaragoza, 50006 Zaragoza, Spain

^c Departamento de Geología y Geoquímica, Universidad Autónoma de Madrid, 28049 Madrid, Spain

^d Paleomagnetic Laboratory CCITUB - Geosciences Barcelona (Geo3Bcn), CSIC, 08028 Barcelona, Spain

ARTICLE INFO

Article history:

Received 11 February 2021

Received in revised form 19 November 2021

Accepted 26 November 2021

Available online 2 December 2021

Keywords:

Magnetic fabrics

Volcaniclastic

Volcanism

Late Carboniferous-Permian

Pyrenees

ABSTRACT

The aim of this work is the application of the anisotropy of magnetic susceptibility (AMS) to the study of volcanic materials from the Late Carboniferous-Permian Cadí basin (southern Pyrenees) in order to (i) explore the limits of this technique in ancient volcanic materials that have undergone strong chemical alteration and a complex tectonic evolution and (ii) provide new insights on the deposition of volcanic materials in this tectonically controlled sedimentary basin. To establish a comparison with the petrofabric of rocks, AMS was complemented with observations and orientation analyses at the outcrop scale, in oriented polished blocks and in thin sections under the microscope. High resolution sampling (620 specimens from 56 sites located in five transects along a sequence 150 m thick) allowed to characterize the volcaniclastic and lava flow series. The AMS results show a fairly constant average magnetic lineation oriented WNW-ESE (in situ and tilt-corrected) and two secondary maxima (N-S to NE-SW in some areas). The magnetic mineralogy analyses indicate the contribution of paramagnetic and ferromagnetic (magnetite, T_c 580 °C) phases to susceptibility. The magnetic fabric has a close relationship with the spatial distribution and orientation of the mineral and grain components of the studied rocks, mainly controlled by depositional processes, with a negligible contribution of the tectonic imprint. Therefore, the magnetic lineation (i.e. K1 axes) can be reliably used as a paleoflow indicator. Nevertheless, it was not possible to establish a clear correspondence between lithological and magnetic fabric types. The results obtained indicate that the AMS approach represents a powerful tool to infer the paleoflow pattern in ancient volcanic and volcaniclastic rocks, even under a priori unfavourable conditions.

© 2021 The Author(s). Published by Elsevier B.V. This is an open access article under the CC BY-NC-ND license (<http://creativecommons.org/licenses/by-nc-nd/4.0/>).

1. Introduction

The Late Palaeozoic (Late Carboniferous and Permian), together with the Late Cretaceous, is one of the stages with stronger volcanic activity at planetary scale. This activity concentrated in particular areas of the Earth, where volcanic products were either linked to fissural magmatism or volcanic cones (e.g. He et al., 2007; Jerram et al., 2016). In the western part of the Late Palaeozoic Variscan orogen (Iberian arc, Pastor-Galán et al., 2012, 2015, and references therein), Late Carboniferous-Permian volcanic deposits are well preserved in some parts of the Iberian Chain and the Pyrenees (Bixel and Lucas, 1983; Calvín et al., 2014; Lago et al., 2004, 2005; Pereira et al., 2014; Van der

Voo, 1969). In particular, the Pyrenean range preserves a good record, exceptional outcrops and a variety of volcanic products (e.g. Gisbert, 1981; Martí, 1986). This volcanism has been linked to Late-Variscan crustal- or lithospheric-scale faults (Aldega et al., 2019 and references therein; Arthaud and Matte, 1977) and in some cases it could also represent the link between the Variscan and Cimmerian cycles (Druguet et al., 2014; Pereira et al., 2014; Pereira et al., 2015). Volcanic products were deposited in small, variably spaced intra-mountain basins (e.g. Gisbert, 1981; Valero-Garcés, 1990) (Fig. 1A). These basins show a complex tectonic evolution, whose analysis is difficult because depositional features are frequently masked by the subsequent Pyrenean (Late Cretaceous to Cenozoic) compression. Furthermore, most of these basins were inverted and/or transported southwards in the hangingwall of basement thrust sheets (e.g. Izquierdo-Llavall et al., 2013b; Saura, 2004). Many geodynamic aspects remain poorly understood and are

* Corresponding author.

E-mail address: anasimon@unizar.es (A. Simón-Muzás).

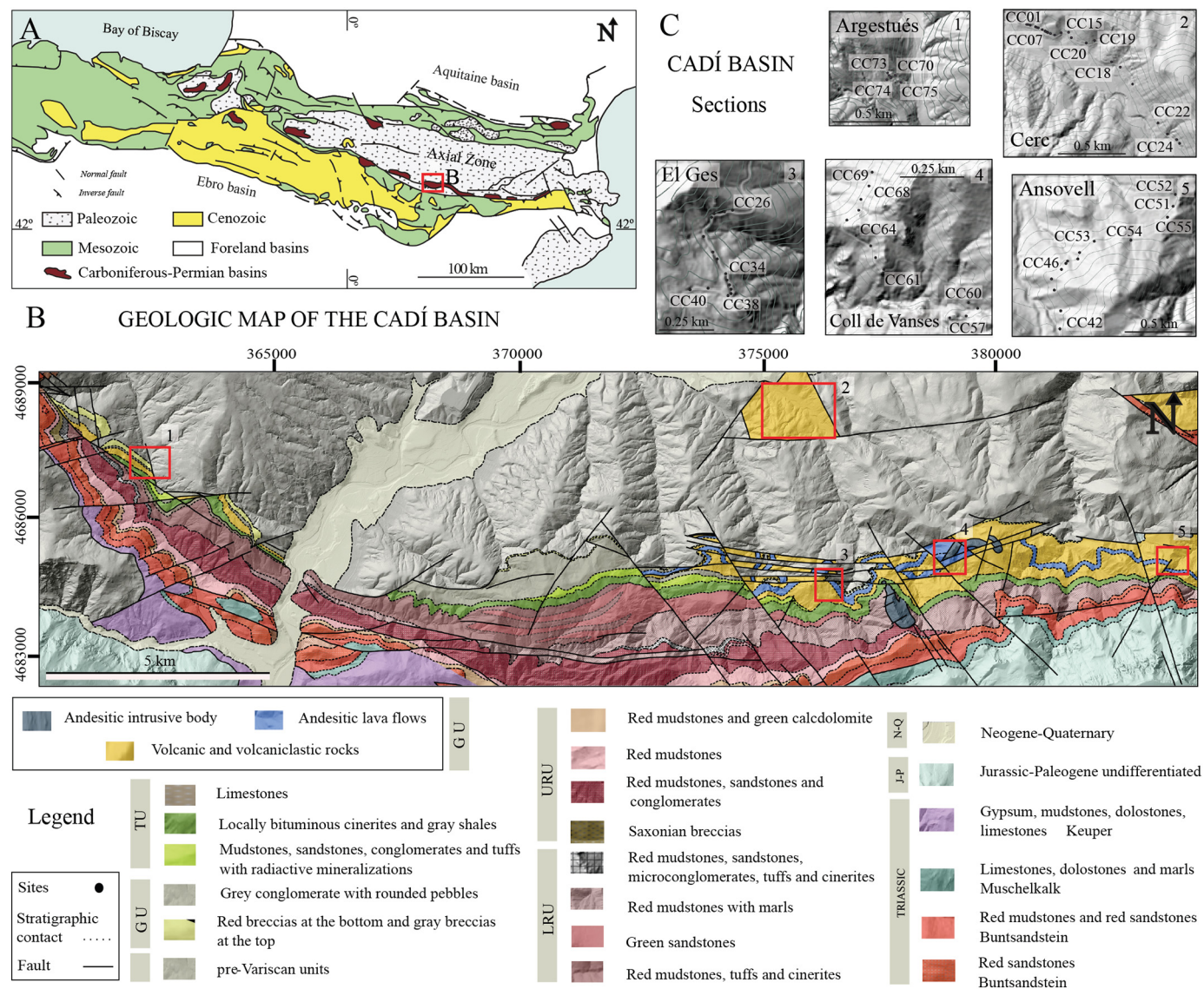


Fig. 1. A) Geological map of the Pyrenees and situation of the Carboniferous-Permian basins; the Cadí basin squared in red (Modified from Izquierdo-Llavall et al., 2013b). B) Geological map digitized from Gisbert (1981). Red squares indicate position of the studied sections represented in C). C) Studied sections and position of sampling sites: 1) Argestués, 2) Cerc, 3) El Ges, 4) Coll de Vanses and 5) Ansovell. In the legend: GU - Grey Unit. TU - Transition Unit. LRU - Lower Red Unit. URU - Upper Red Unit. J-P - Jurassic-Paleogene. N-Q - Neogene-Quaternary.

nevertheless crucial to understand the geodynamic consequences of the Pangea amalgamation and the Late Palaeozoic Pangea break-up during the progressive fracturing of the Variscan chain.

The Cadí basin is one of the most remarkable Late Carboniferous-Permian basins of the Pyrenean range because of its exceptional exposures and the diversity of volcanic products (Fig. 1B). Lava flows and volcanoclastic materials reflected a variety of temperatures and depositional conditions that occurred during their sedimentation (Gisbert, 1981; Martí, 1986). Classical structural techniques applied to lava flows and volcanoclastic materials can help to decipher their flow patterns and to locate the possible source areas (Bullock et al., 2018; Cas et al., 2011; Coward, 1980; Schmincke, 1967; Smith, 2002; Waters, 1960). However, these techniques are time-consuming and difficult to apply depending on the outcrop conditions. Several decades ago, the application of the analysis of the anisotropy of magnetic susceptibility (AMS) to volcanic rocks emerged successfully (e.g. Cagnoli and Tarling, 1997; Cañón-Tapia et al., 1995, 1996; Cañón-Tapia, 2004b; Ellwood, 1978; Incoronato et al., 1983; Knight et al., 1986; MacDonald et al., 2012; Ort et al., 2015; Paquereau-Lebti et al., 2008; Porreca et al.,

2003; Soriano et al., 2008; Urrutia-Fucugauchi et al., 1984). It represents a fast, simple and verifiable technique that helps to decipher the internal texture of lava flows and pyroclastic deposits and can therefore indicate the flow directions and in some cases the flow sense at different scales (e.g. Cañón-Tapia, 2004b). AMS application in volcanic and pyroclastic rocks offers therefore a reliable, statistically sound determination of magma source and the possibility of reconstructing the evolution of the volcanic processes along time. However, it is important to take into account the limitations of AMS deriving from the possible existence of composite magnetic fabrics and/or mineral artifacts (Ort et al., 2015).

In this work we apply AMS and rock magnetism techniques as well as classic structural and microstructural analyses to volcanic and pyroclastic materials of the Cadí basin, where flow directions are poorly known. This study will contribute to increase the knowledge of the geodynamic constraints of this Late Palaeozoic basin, strongly controlled by tectonics and volcanism. In fact, several hypotheses, favouring (i) a volcanic-related origin with subordinate control by regional faults (Martí and Mitjavila, 1987, 1988), or a purely tectonic control to sedimentation and volcanic product deposition, either by (ii) strike-slip

faults of Pyrenean direction associated to secondary, normal perpendicular systems (Gisbert, 1981), or (iii) by normal faults defining grabens parallel to the Pyrenean trend and alternation of transtension and transpression (Speksnijder, 1985). Our approach can also give clues for reconstructing the paleoflow pattern and the tectonic context in equivalent Late Carboniferous-Permian basins at the scale of the south-western European peri-Tethyan realm.

2. Geological setting

2.1. The Pyrenean range and the Variscan orogen

The Pyrenean range is a double vergence orogen located at the northern boundary of the Iberian Peninsula. It extends in an E-W direction, from the Mediterranean Sea to the Atlantic Ocean, and is integrated in the Alpine Chain system (e.g. Muñoz, 2019 and references therein). This range represents the suture between the European and Iberian plates and was formed between the Late Cretaceous and the earliest Miocene. The Pyrenean range is composed of a set of thrust units with a dominant southern vergence in its southern side. It is traditionally subdivided in three zones, defined by Mattauer (1968): North Pyrenean Zone, Axial Zone where the Palaeozoic basement crops out, and the South Pyrenean Zone. The Pyrenean range is the result of two orogenies, Variscan and Alpine, that occurred during the Palaeozoic and Cenozoic, respectively, and two main rift-postrift Late Palaeozoic-Mesozoic cycles affecting the Variscan basement (e.g. Barnolas and Pujalte, 2004; Capote et al., 2002). The Alpine orogeny lasted in the Pyrenees from the Late Cretaceous to the Miocene due to the convergence between the European and Iberian plates (e.g. Muñoz, 1992).

The Variscan orogenic belt resulted from the collision between Laurussia and Gondwana and formed the Late Palaeozoic Pangea supercontinent (e.g. Franke, 2000; Gutiérrez-Alonso et al., 2011; Murphy et al., 2009). The Variscan evolution included, according to different authors, the development of the Cantabrian orocline (Gutiérrez-Alonso et al., 2011; Johnston et al., 2013), the Pangea self-subduction (Gutiérrez-Alonso et al., 2008) or the transient continental magmatic arc developed in the Eurasian convergent plate margin above the subducted Paleotethys oceanic plate related to the Cimmerian cycle (Pereira et al., 2017). The late- to post-Variscan orogenic evolution was characterized by extension and thinning associated with orogenic collapse (e.g. Burg et al., 1990; Faure et al., 2002). A dextral-transensional to extensional regime affected the Variscan belt during the Late Carboniferous and Permian (e.g. Burg et al., 1994; Van Den Driessche and Brun, 1989) except in some parts of the belt, where a contractional deformation previous to the deposition of the Triassic basins has been registered (Pereira and Gama, 2017). In the Pyrenees, this stage is recorded by syn-tectonic sedimentary sequences deposited from probably Kasimovian (Pereira et al., 2014) to Middle-Permian, Wordian, (Mujal et al., 2016) in a set of small intra-mountain E-W elongated basins. These basins show similar subsidence patterns (i.e. in terms of the distribution of the depocenters and deposits), and have been interpreted as graben or half-graben continental troughs (e.g. Bixel and Lucas, 1983; Gisbert, 1981; Martí, 1986). This process was coeval with an exceptional episode of intraplate magmatism characterized by the emplacement of thick volcanic and sub-volcanic bodies (sometimes hundreds of meters thick) (e.g. Gisbert, 1981; Lago et al., 2004; Martí, 1986). Eruptions were coeval with chronological link between deep-seated processes in magma chambers (i.e. granodiorites and dacitic dykes located to the North of these basins in present day coordinates) and they (i.e. rhyolitic ignimbrites and andesitic flows) has been recently established (e.g. Pereira et al., 2014).

At present, most Pyrenean Late Carboniferous-Permian basins are distributed along the southern edge of the Axial Zone, limited to the South by Alpine thrusts that acted as normal or wrench faults during the Late Carboniferous-Early Permian (Gisbert, 1981; Saura and Teixell, 2006). They are aligned in a discontinuous WNW-ESE (i.e.

Pyrenean trend) band at constant intervals of about 32–38 km (Fig. 1A). A previous AMS analysis was carried out in the Castejón-Laspaules basin, located to the West of the Cadí basin, in equivalent Late Carboniferous-Permian pyroclastic and andesitic rocks, obtaining a NW-SE-trending flow pattern (Izquierdo-Llavall et al., 2013b). Bixel and Lucas (1983) describe the existence of volcanic calderas and dome structures in the eastern sector of the Cadí basin (eastwards of the studied area) that could control the magma ascent and the setting of volcanic buildings.

2.2. Structure of the Cadí basin

The Cadí basin is a WNW-ESE basin, approximately 30 km long, located in the Eastern Pyrenees (Fig. 1A). During the Alpine orogeny, this basin was incorporated in the Orri unit (Muñoz, 1992; Saura and Teixell, 2006), a basement south-vergent thrust sheet involving Palaeozoic materials and an unconformable Triassic cover that forms part of the antiformal stack of the Pyrenean Axial Zone (e.g. Muñoz, 1992). The Cadí basin is an example of intra-mountainous basin where Late Carboniferous-Permian series are at present aligned along an E-W continuous outcrop and reach thicknesses of several hundreds of meters with a good preservation and exposure of the volcanic materials (Gisbert, 1981; Martí, 1986). The basin has been interpreted as an asymmetric graben limited by extensional faults to the north and south (Saura and Teixell, 2006), although none of its bounding faults are exposed at present. The Late Carboniferous-Permian rocks of the Cadí basin crop out along a south-dipping monocline (average dips between 30 and 65° S) interpreted as the southern limb of a basin-scale anticline associated with the Alpine Orri thrust (Saura and Teixell, 2006). In a closer look, (between traverses 3 and 4, Fig. 1), hectometer-scale WNW-ESE asymmetric folds can be also inferred from the geological map (Gisbert, 1981). There are also other outcrops (Cerc section, Fig. 1C), where Late Carboniferous-Permian rocks describe a syncline in the downthrown side of a Miocene normal fault (Saura, 2004). This small graben is surrounded by Ordovician rocks and is tightly folded with an ENE-WSW (N055E) axis. A pervasive set of NW-SE faults with displacements between 10 and 100 m can be also inferred from the cartographic distribution of outcrops (see also Gisbert, 1981).

2.3. Stratigraphy

The stratigraphic subdivision of the Late Palaeozoic continental successions in Iberia is still under discussion and, because of their continental origin, most of them lack precise dating (e.g. Gretter et al., 2015; Lloret et al., 2018; Mey et al., 1968; Nagtegaal, 1969). Gretter et al. (2015) have recently done a detailed sedimentological and stratigraphical analysis of the Late Palaeozoic sequences cropping out in the Cadí basin and adjacent basins in the context of the western peri-Tethyan palaeogeography. In this work, we follow the stratigraphic subdivision proposed by Gisbert (1981) of the Late Carboniferous-Permian rocks in the Southern Pyrenees (Fig. 1B): Grey Unit, Transition Unit, Lower Red Unit and Upper Red Unit. The Grey Unit (GU) lies unconformably on the Variscan basement materials. This unit starts with breccias, sandstones, conglomerates, grey siltstones and layers of coal. This sedimentary sequence passes laterally to volcano-sedimentary and pyroclastic rocks with interbedded andesitic lavas. The Transition Unit (TU) is characterized by conglomerates, sandstones and siltstones commonly containing ostracods, charophytes and stromatolites (the latter linked to ankeritic limestones) at its top. In this unit, sedimentary rocks present frequent lateral changes to pyroclastic rocks with dacitic interbedded lavas. The Lower Red Unit (LRU) is mainly composed by siltstones, sandstones, acid tuffs and red volcanoclastic microconglomerates. In the Cadí basin these sedimentary rocks interfinger with ignimbrites and interbedded banded rhyolites. Finally, the Upper Red Unit (URU) contains red conglomerates, sandstones, siltstones with carbonate nodules and

lacustrine deposits. These rocks are arranged in two sequences with interbedded volcanic bodies at the bottom.

This work focuses exclusively on volcanic and volcanoclastic rocks from the GU and TU of the Cadí basin. All the sampling sites are located in the Grey Unit (GU), except (perhaps) for sites CC75 and CC74 (Argestués section) that possibly belong to the Transition Unit (TU) because a paleosol was found below their stratigraphic position. According to Gisbert (1981), the GU deposited in a sedimentary environment with small alluvial fans at the basin borders and small lakes developed between volcanic structures. The TU corresponds to fluvial (ephemeral rivers) and lacustrine environments.

To identify the different lithological types in the volcanoclastic rocks, White and Houghton's (2006) classification was followed. According to this classification ignimbrites and a lahar (containing carbonized logs) are included in pyroclastic deposits.

3. Methodology

The methodology used includes field work and sampling planification and execution (performed after careful analysis and re-elaboration of existing geological maps by means of aerial images), laboratory work (here including magnetic mineralogy analysis, AMS analyses and thin section observations under the microscope), and interpretation of the whole dataset, especially including stereonet representations. Special attention was paid to check if (1) there is a relationship of the magnetic fabric with the defined lithological type or (2) a variable spatial pattern that would be an indicator of a preferential direction of flow or deformation.

3.1. Sampling

The sampling campaigns were designed to carry out five detailed transects in N-S and NE-SW directions in the Cadí basin with a total of 56 sampling sites: Argestués (4 sites), Cerc (17 sites), El Ges (7 sites), Coll de Vanses (13 sites) and Ansovell (15 sites) sections (see Fig. 1B, C and Table 1 for location). The sampling products correspond to the oldest Late Carboniferous-Permian rocks, i.e. the volcanic and volcanoclastic rocks of the Grey and Transition Units. Three lithological types were sampled; 1) autoclastic deposits (12 sites), 2) andesitic lava flow (22 sites), and 3) pyroclastic deposits, here including ignimbrites (22 sites).

The samples were directly obtained in the field as cylindrical cores with gasoline and battery-powered drill machines cooled with water (33 sites) or as oriented blocks taken with extraction tools (23 sites). In the block sites, one to four blocks per site were taken and in the 33 drilled sites an average value of eight cores per site was obtained. A higher number of samples (one to two samples per core) was obtained to ensure the representativeness of the AMS results, as proposed in the studies of other intrusive rocks (Pueyo et al., 2004). Sampling was conditioned by the quality and the distribution of the outcrops. All samples were oriented with a magnetic or a solar compass, and sampling localities were positioned with a GPS. Oriented cores and blocks were cut to 2.1 cm-long, 2.5 cm-diameter standard cylinder specimens and 2 cm-edge standard cube specimens, respectively, using a radial saw and a diamond drill bit (non-magnetic steel). Bedding or flow planes were measured in most sampling sites. A total of 620 standard specimens (averaging 11 specimens per site) were obtained.

3.2. Magnetic mineralogy

Four types of analyses were performed to determine the magnetic mineralogy of sampled rocks: 1) temperature-dependent susceptibility curves at room temperature and at low temperature (~77 K), 2) temperature-dependent induced magnetization curves, 3) isothermal remanent magnetization (IRM) and backfield acquisition curves and 4) hysteresis loops. These experiments were carried out to characterize

the main magnetic carriers of the AMS and their relative contribution (i.e. ferromagnetic versus paramagnetic fraction).

Temperature-dependent susceptibility curves were carried out in seven samples from different sites, except in one case (CC35), where lithological variability required two curves. The selection criterion was based on the magnetic fabric results (susceptibility value, k) obtained with the AMS measurements. The KLY-3S Kappabridge combined with a CS-3 furnace (temperature range 40–700 °C) and the software SUSTE (AGICO Inc., Czech Republic) were used for this analysis. Moreover, two samples were selected to perform temperature-dependent susceptibility curves at low temperatures (~77 K) with the aim of ensuring their main paramagnetic behaviour. For this purpose, the samples were cooled in liquid nitrogen and analysed in the CS-L unit of the KLY-3S Kappabridge using the software SUSTEL (AGICO Inc., Czech Republic). The temperature-dependent susceptibilities curves were represented using the software Cureval 8 (Chadima and Hrouda, 2012).

Temperature-dependent induced magnetization curves (up to 700 °C in constant field of 38 mT), isothermal remanent magnetization (IRM) and backfield acquisition curves (progressively increasing fields up to 1 T and then reverse fields of increasing intensity) and hysteresis loops (at room temperature with a maximum applied field of 1 T) were performed by means of a magnetic variable field translation balance (MMAVFTB, Petersen Instruments) in the Paleomagnetism Laboratory of the University of Burgos, Spain, on representative specimens of pyroclastic deposits, autoclastic deposits and lava flows (CC23–4A, CC35–2A and CC61–9A, respectively) from three different traverses. The data were processed using the software Analyzer 1.0 (Leonhardt, 2006).

3.3. Analysis of RT-AMS

Anisotropy of magnetic susceptibility (AMS) measurements at room temperature (RT-AMS) were conducted at the Magnetic Fabrics Laboratory of the University of Zaragoza, Spain, using a Kappabridge KLY-3S (AGICO Inc., Czech Republic). The AMS is a technique that defines the spatial variation of magnetic susceptibility (k) by applying a low intensity magnetic field in different orientations around a core or cubic specimen. Magnetic susceptibility (k) of a rock is the relationship between the applied magnetic field (H) and the induced magnetization (M), $M = k \cdot H$. Magnetic susceptibility (k) is dimensionless (in the International System) and it can be expressed as a second-rank symmetric tensor and represented geometrically by an ellipsoid with three orthogonal principal axes $K_1 > K_2 > K_3$ (see Tarling and Hrouda, 1993 for further details). AMS, and therefore the magnetic ellipsoid orientation, depends on the preferred orientation of the magnetic carriers within the rock (i.e., ferromagnetic, paramagnetic and diamagnetic minerals, Borradaile and Jackson, 2004). The magnetic susceptibility ellipsoid was firstly defined by Nye (1957) and three parameters are typically used for its characterization (Jelinek, 1981); (i) mean susceptibility (K_m or K_{mean}), expressed as $K_m = (K_1 + K_2 + K_3)/3$, (ii) corrected anisotropy degree (P_j) expressed as $\ln(P_j) = \sqrt{2}((\ln(K_1/K))^2 + (\ln(K_2/K))^2 + (\ln(K_3/K))^2)^{1/2}$, and (iii) shape parameter (T) expressed as $T = 2(\mu_2 - \mu_3)/(\mu_1 - \mu_3) - 1$ where $\mu_1 = \ln K_1$, $\mu_2 = \ln K_2$, $\mu_3 = \ln K_3$ y $\mu_m = (\mu_1 + \mu_2 + \mu_3)/3$. In this work we will consider the $T = 0.2$ and $T = -0.2$ values as the boundaries between oblate (s.l.) ellipsoids, triaxial ellipsoids and prolate (s.l.) ellipsoids, but in some cases where the analysed sites present particular patterns of spatial distribution of the principal axes, regardless of the T value, we take into account its geometry for the classification. This is shown later on (see Fig. 5) where studied sites are also classified according to their lithological type. Because of the different volume of cylinders and cubes, a volume correction (1.37 ratio) was applied for the latter in the calculation of the bulk susceptibility.

The susceptibility tensor was calculated, including statistical confidence angles ($e12$, $e13$, $e21$, etc...), with the software SUSAR (AGICO Inc., Czech Republic). The AMS values for all specimens from each site

Table 1
Magnetic parameters (AMS) for the sampling sites in the Cadí basin.

	Site	ETRS 89 UTM 31		N	Lithology	K1 in situ	Conf. Ang.	K3 in situ	Conf. Ang.	Km (10 ⁻⁶)	e (10 ⁻⁶)	Pj	e	T	e	Ellipsoid type	S0 (Dip direction)
		Latitude (X)	Longitude (Y)														
Cerc	CC1	375,347.19	4,688,784.81	9	lava flow	180/40	12/5	86/04	16/10	289	55.57	1.011	0.004	−0.368	0.125	prolate	174/30
	CC5	375,418.01	4,688,763.67	7	pyroclastic	202/46	1.6/0.9	053/40	6.6/0.4	1004	73.53	1.024	0.003	−0.372	0.152	prolate	174/30
	CC6	375,427.19	4,688,761.06	9	autoclastic	149/49	56/7	332/42	22/06	404	128.9	1.008	0.003	−0.037	0.312	oblate	174/30
	CC7	375,455.72	4,688,748.34	9	pyroclastic	279/31	9/4	174/23	20/3	365	46.54	1.007	0.002	0.155	0.271	triaxial	153/28
	CC8	375,475.6	4,688,740.21	12	autoclastic	096/23	14/05	213/47	62/13	518	265.9	1.012	0.004	−0.287	0.405	prolate	153/28
	CC10	375,489.3	4,688,731.75	8	pyroclastic	038/27	37/13	238/61	25/02	255	39.3	1.011	0.004	0.394	0.52	oblate	100/20
	CC13	375,542.41	4,688,710.92	22	lava flow	254/21	30/9	027/61	15/9	262	32.71	1.007	0.002	0.063	0.448	oblate	205/36
	CC14	375,586.03	4,688,726.58	13	pyroclastic	227/58	11/06	116/13	42/5	338	77.72	1.008	0.003	−0.092	0.220	prolate	194/42
	CC15	375,638.34	4,688,730.21	10	lava flow	274/23	20/13	076/66	37/16	222	74.52	1.006	0.002	0.048	0.215	triaxial	–
	CC16	375,667.53	4,688,684.82	20	lava flow	331/41	16/09	186/43	12/09	485	109	1.01	0.008	0.188	0.360	oblate	050/36
	CC18A	375,819.43	4,688,672.79	5	pyroclastic	228/86	52/23	111/02	24/12	705	608	1.022	0.011	0.295	0.449	oblate	300/45
	CC18B	375,819.43	4,688,672.79	6	pyroclastic	291/13	15/07	188/46	11/03	267	50.57	1.014	0.004	0.48	0.262	oblate	300/45
	CC19	375,937.86	4,688,524.63	8	lava flow	198/58	07/04	070/21	12/05	218	52.17	1.01	0.002	0.186	0.382	triaxial	300/45
	CC20	375,997.7	4,688,488.47	6	pyroclastic	310/04	25/21	041/05	36/12	258	92.63	1.01	0.004	−0.123	0.342	triaxial	322/44
	CC22	376,259.48	4,688,099.64	9	lava flow	185/37	07/03	339/50	08/04	3880	426.2	1.031	0.003	0.022	0.223	triaxial	165/33
	CC23	376,324.71	4,688,023.29	16	pyroclastic	123/30	09/07	309/60	33/08	1335	700.5	1.017	0.009	−0.162	0.331	prolate	115/40
	CC24	376,389.55	4,687,984.94	15	pyroclastic	101/56	27/15	220/18	49/15	328	146.5	1.013	0.007	0.139	0.471	triaxial	092/60
	CC26	376,514.62	4,684,781.72	16	pyroclastic	309/04	24/14	161/86	35/21	218	56.92	1.013	0.004	0.146	0.490	oblate	330/30
	CC34	376,492.95	4,684,501.86	11	pyroclastic	064/46	09/08	329/04	57/08	800	467.7	1.014	0.003	−0.542	0.139	prolate	170/72
	CC35	376,501.7	4,684,483.38	19	autoclastic	094/05	29/08	185/11	12/08	329	58.62	1.01	0.002	0.323	0.285	oblate	180/90
El Ges	CC36	376,508.86	4,684,464.26	13	pyroclastic	090/20	25/06	358/07	16/09	1053	488	1.02	0.008	−0.131	0.492	triaxial	180/80
	CC37	376,508.25	4,684,448.06	18	lava flow	276/02	18/07	15/80	13/07	575	102	1.045	0.008	−0.329	0.178	prolate	180/90
	CC38	376,496.13	4,684,438.83	8	autoclastic	090/08	16/10	192/57	27/07	1121	585	1.024	0.01	−0.177	0.297	triaxial	180/90
	CC41	376,311.15	4,684,394.55	14	pyroclastic	285/4	14/8	15/09	31/12	1278	231	1.018	0.005	−0.021	0.264	triaxial	210/32
	CC42	383,130.08	4,684,809.1	19	lava flow	114/27	19/8	253/56	27/5	399	180.6	1.007	0.002	−0.147	0.381	triaxial	204/45
	CC43	383,133.50	4,684,885.79	9	pyroclastic	266/15	7/4	115/73	27/4	441	53.62	1.008	0.001	−0.018	0.48	prolate	–
	CC44	383,106.44	4,684,973.54	9	lava flow	252/24	18/2	1/36	9/1	6784	2446	1.022	0.003	−0.31	0.201	prolate	210/48
	CC45A	383,094.11	4,685,020.4	7	lava flow	318/02	12/7	225/58	39/4	699	60.47	1.022	0.009	−0.169	0.232	triaxial	190/65
	CC45B	383,094.11	4,685,020.4	8	lava flow	99/38	4/0	194/07	8/2	374	29.53	1.005	0	0.017	0.038	triaxial	190/65
	CC46	383,136.68	4,685,061.45	6	autoclastic	310/37	14/7	150/51	13/3	384	27.3	1.005	0.002	−0.171	0.353	triaxial	235/48
Ansovell	CC48	383,162.32	4,685,096.34	10	lava flow	101/33	22/8	288/56	24/4	1894	4920	1.016	0.002	0.145	0.429	triaxial	–
	CC49A	383,206.16	4,685,105.28	8	lava flow	101/55	4/1	265/34	58/4	938	115	1.014	0.003	−0.272	0.447	prolate	295/35
	CC49B	383,206.16	4,685,105.28	8	lava flow	133/62	72/3	313/28	6/2	771	44.38	1.018	0.005	0.77	0.094	oblate	295/35
	CC50	383,213.46	4,685,132.81	9	lava flow	98/47	22/10	269/43	22/9	325	52.53	1.008	0.002	0.036	0.175	triaxial	190/75
	CC51	383,609.54	4,685,328.82	7	pyroclastic	005/32	59/38	108/19	52/37	2147	478.9	1.055	0.019	−0.194	0.285	triaxial	169/26
	CC52	383,619.36	4,685,379.19	5	pyroclastic	158/61	19/08	057/06	33/07	4440	852.4	1.04	0.009	0.037	0.601	oblate	250/78
	CC53	383,275.42	4,685,180.32	10	pyroclastic	273/20	4/2	180/8	13/3	338	30.28	1.004	0.001	−0.352	0.237	prolate	235/85
	CC54	383,430.49	4,685,184.96	11	autoclastic	260/26	5/3	44/59	9/5	632	54.8	1.013	0.003	0.126	0.113	triaxial	270/78
	CC55	383,585.93	4,685,282.34	11	autoclastic	14/32	12/4	109/9	10/4	386	128	1.009	0.001	0.039	0.226	triaxial	270/78
	CC57	379,223.56	4,684,827.07	14	lava flow	240/23	16/09	051/67	20/08	501	284.8	1.026	0.01	−0.108	0.312	triaxial	160/52
Coll de Vanses	CC58	379,291.87	4,684,834.9	10	autoclastic	182/34	29/08	346/55	28/11	3076	2630	1.023	0.009	−0.254	0.257	prolate	180/47
	CC59	379,340.49	4,684,867.05	12	lava flow	058/13	31/10	172/61	33/10	525	98.78	1.034	0.01	0.169	0.527	triaxial	180/47
	CC60	379,302.23	4,684,890.47	15	pyroclastic	272/02	15/08	175/70	10/08	1045	352.3	1.027	0.007	−0.08	0.311	triaxial	180/47
	CC61	378,948.31	4,685,029.97	15	lava flow	092/24	06/03	347/30	06/03	322	28.43	1.011	0.001	−0.032	0.149	triaxial	160/60
	CC62	378,913.47	4,685,079.55	22	autoclastic	135/59	18/13	022/13	72/14	1044	994.1	1.024	0.024	−0.051	0.412	prolate	160/55
	CC63	378,893.05	4,685,129	7	autoclastic	274/06	09/05	180/31	31/04	1873	3196	1.014	0.006	0.084	0.368	triaxial	–
	CC64	378,831.97	4,685,172.6	11	lava flow	251/44	14/07	006/24	20/07	460	137.6	1.012	0.002	−0.246	0.406	prolate	130/86
	CC65	378,793.6	4,685,237.35	8	autoclastic	102/08	21/04	010/17	26/05	563	175.9	1.012	0.007	0.257	0.518	oblate	180/65
	CC66	378,843.03	4,685,278.37	11	lava flow	226/54	43/14	109/18	73/16	2025	2547	1.01	0.003	−0.312	0.305	prolate	205/54
	CC67	378,852.14	4,685,323.97	9	lava flow	115/13	17/10	012/47	15/06	549	225	1.018	0.006	0.051	0.257	triaxial	177/42
Argestués	CC68	378,885.43	4,685,379.93	13	lava flow	122/15	45/04	029/10	08/05	302	50.47	1.017	0.005	−0.084	0.345	oblate	183/63
	CC69	378,899.21	4,685,437.78	6	autoclastic	055/12	19/08	146/05	10/04	1564	236	1.026	0.004	0.338	0.347	oblate	194/29
	CC70	362,096.11	4,687,048.53	13	pyroclastic	288/04	26/03	25/57	04/02	181	8.68	1.015	0.005	0.727	0.727	oblate	207/38
	CC71	362,073.35	4,687,035.42	9	pyroclastic	288/20	11/03	160/59	31/05	149	14.75	1.009	0.002	−0.191	0.356	triaxial	180/31
	CC74	362,035.35	4,687,023.28	5	pyroclastic	124/09	17/09	234/65	60/12	65	3.57	1.007	0.005	0.07	0.25	triaxial	202/35
	CC75	362,140.21	4,686,998.23	20	pyroclastic	070/24	09/06	306/52	10/06	202	21.71	1.015	0.004	0.419	0.247	oblate	200/45

N: number of specimens; Lithology: classification in lithological type; K₁ and K₃-mean (trend and plunge) of the magnetic lineation and of the pole to the magnetic foliation (Jelinek, 1977) in situ; Conf Ang: major and minor semi-axes of the 95% confidence ellipse (Jelinek, 1977); K_m: magnitude of mean magnetic susceptibility (10⁻⁶ SI); Pj: corrected anisotropy degree (Jelinek, 1981); T shape parameter (Jelinek, 1981); e: standard deviation; Ellipsoid type: magnetic susceptibility ellipsoid type; S0: bedding plane (dip direction/dip).

were processed and represented using the software *Anisoft 5.1.03* (Chadima and Jelinek, 2019).

3.4. Analysis of LT-AMS

The paramagnetic behaviour is exponentially enhanced at low temperatures according to the Curie-Weiss law: $K_p = C/T - \theta$; K_p is the paramagnetic susceptibility, C is a constant and θ is the paramagnetic Curie temperature (T_c) (see, e.g. Oliva-Urcia et al., 2009, 2011 and references therein). To isolate the paramagnetic subfabric from the total

fabric, five sites from different transects (5 to 6 specimens per site), were analysed at low temperature in the Kappabridge KLY-3S. A thermal protection was integrated around the measuring coil to protect the instrument from the cooled samples (~77 K) as in Issachar et al., 2016. The low-temperature-AMS (LT-AMS) measurement routine includes an 1-h cooling of the samples at 77 K by immersion in liquid nitrogen and measurements in the four positions required by the KLY-3S. Between each position, the analysed specimen was immersed again 10 min in liquid nitrogen. A pure paramagnetic sample measured at low temperature (77 K) must show an increase of its susceptibility of

approximately 3.8 times with respect of its susceptibility at room temperature (Ihmlé et al., 1989) but when ferromagnetic s. l. minerals are present this ratio diminishes.

3.5. Image analysis and petrographic study

The purpose of these analyses is to compare the magnetic fabric results with the preferred mineral orientations and structures (rock fabric). The petrographic study was carried out at three scales: mesoscale analysis at outcrop scale, macroscopic study in oriented polished blocks and finally microscopic analysis in oriented thin sections. The image analysis of mineral grains was performed in five samples (sites CC05, CC06, CC34, CC44, CC70). These samples were selected in order for the three lithological types and the different transects studied to be represented. For each oriented block, 2D orientation analyses were performed in thin sections (microstructural scale) and polished cuts (mesostructural scale), in two perpendicularly oriented planes. Preferred textural orientations, or AMS results (when crystals or grains were not visible) were used as a guide for tracing the perpendicular-to-foliation, parallel to lineation plane and the perpendicular-to-foliation, perpendicular-to-lineation plane. *ImageJ* software (Schneider et al., 2012) was used to quantify the preferred shape orientations of the different components (Fe-oxides, plagioclases, mafic minerals, pyroxenes and amphiboles, and mineral agglomerates) defining the petrofabric of the studied samples.

3.6. Microstructural study

A systematic microstructural analysis was performed to better constrain the contribution of the tectonic imprint to the overall measure of AMS. A total of 56 thin sections, one for each site, were analysed under the microscope. Thin section planes are perpendicular to the magnetic foliation (i.e. they contain K_{\min} axes) and parallel to the magnetic lineation (i.e. they contain K_{\max} axes). The orientation of the thin sections was done according to the application of the classical stereographic projection techniques in Structural Geology (see Phillips, 1977).

To decipher the influence of the tectonic imprint in the studied rocks, a qualitative classification of the thin sections (and hence the sampling sites) was performed. This classification takes into account the presence or absence of tectonic structures (e.g. tectonic foliation, microfaults or crushed clasts), and the modification of the original orientation of grains (primary fabrics) due to tectonic, secondary features. Type A includes thin sections that do not show any tectonic overprint; Type B groups thin sections that present localized, no-pervasive foliations (e.g. rough cleavage defined by iron oxides); Type C includes thin sections that show tectonic features such as fractured or shear clasts or more pervasive foliation; finally, Type D corresponds to thin sections with a strong tectonic imprint: penetrative foliations, mineral grains reorientations associated with this foliation, microfaults and sheared clasts. We have paid specific attention to differentiate those foliations of primary origin (i.e. formed during the deposition of ignimbrites), from the tectonic ones. Fortunately, orientation of regional cleavage also helps in this task because in the southern border of the Axial Zone of the Pyrenees shows a systematic northwards dip (Izquierdo-Llavall et al., 2013a), opposite to the dip of primary foliation or bedding in most sites.

4. Results

4.1. Rock magnetic characterization

Almost all temperature-dependent susceptibility curves show that magnetic mineralogy consists of a mixture of paramagnetic and ferromagnetic phases (Fig. 2). The paramagnetic behaviour can be inferred from the concave-hyperbolic shape at the beginning of the heating

curves (Curie-Weiss law, e.g. Parés and Van der Pluijm, 2002) (Fig. 2B, C and D). Following Hrouda, 1994, Hrouda et al., 1997 method, the paramagnetic contribution to the total susceptibility has been estimated between 45% (sample CC26-2C) and 100% (samples CC35-IRM). In the remaining five samples, the paramagnetic contribution is dominant, ranging between 71% and 92%.

The ferromagnetic behaviour is pinpointed by the abrupt drop in the heating curve between 580 °C and 600 °C (Fig. 2B, C and D) taking into account that the Curie temperature of magnetite is 580 °C (this behaviour is not followed by sample CC35-4B). Furthermore, an abrupt increase in susceptibility at 500 °C evidences the neoformation of magnetite during heating in sample CC26-2C (Fig. 2B). Temperature-dependent susceptibility curves are not reversible, and cooling paths show susceptibilities one order of magnitude higher than heating paths, confirming the formation of ferromagnetic phases during heating (Fig. 2A).

In the temperature-dependent induced magnetization curves (Fig. 3C), there is a drop in the magnetization value at 560 °C and 580 °C (T_c of magnetite) in samples CC61-9A and CC23-4A (much more abrupt) respectively a second, weaker drop at 675 °C (T_c of haematite) in samples CC23-4A and CC35-5B. If we pay attention to the acquisition of isothermal remanent magnetization (IRM) and backfield curves (Fig. 3A and B), in samples CC23-4A and CC61-9A, saturation is not reached at 1 T and in sample CC35-5B, it is reached at 100 mT. The hysteresis loops display a more linear trend in samples CC35-5B and CC61-9A than in sample CC23-4A, which shows a wasp-waisted hysteresis (Fig. 3D).

The mean value of K_m for all sites is 926.84×10^{-6} SI, ranging between 6784×10^{-6} (site CC44, lava flow) and 65×10^{-6} SI (site CC74, pyroclastic deposit). The mode value corresponds to 218×10^{-6} SI. The autoclastic deposits are the only lithological type that do not show K_m values under 300×10^{-6} SI (Table 1). If we pay attention to K_m values for individual data specimens (see Fig. 6C) the mode is rather low, 276.7×10^{-6} SI, although the values range between 44×10^{-6} SI to 9060×10^{-6} SI. The K_m average value is high even though the K_m mode value is low because the histogram is asymmetric towards the highest values.

4.2. Magnetic fabrics: RT-AMS

Regarding the characterization of the magnetic ellipsoid, the corrected anisotropy degree P_j is low in all sampled sites (Table 1), with values typical of weakly deformed sediments ($P_j < 1.1$). The mean value of P_j at the site level is 1.017, with a maximum value of 1.055 (site CC51) and a minimum of 1.004 (site CC53) (Table 1). The parameter T shows triaxial magnetic ellipsoids for most sites (27 sites) despite the wide variability of values (Table 1, Fig. 4 and Fig. 5). K_m - P_j and K_m - T diagrams show no correlation between K_m , P_j or T , or between these three parameters and the sampled lithology (Fig. 4).

A high variability of magnetic fabrics has been obtained independently of the studied section and the stratigraphic position of sites (Table 1). In order to interpret this variety, we have considered P_j and T values (Fig. 6D) from individual specimens for each traverse. The Argestués and El Ges transects show the highest P_j values (in all cases lower than 1.05). In all the studied transects, most of the P_j values are lower than 1.02. There is not a relationship between the lithological type and the P_j and T parameters at sampling site level.

The lithological types do not present a characteristic magnetic fabric type (Fig. 6A and 7). Most sites feature magnetic ellipsoids with a tight clustering of K_3 (Table 1) and 86% of sites show a well-defined magnetic lineation (confidence angle associated with K_1 , $e12 < 30^\circ$). Sites with poorly defined magnetic lineation correspond to lava flows and falling pyroclasts (Table 1). In most sites magnetic lineation (K_1) is located within or close to the measured bedding plane and K_3 axes are clustered around the bedding pole, both considering site means (Fig. 6B) or individual samples (Fig. 7). After bedding restoration, the

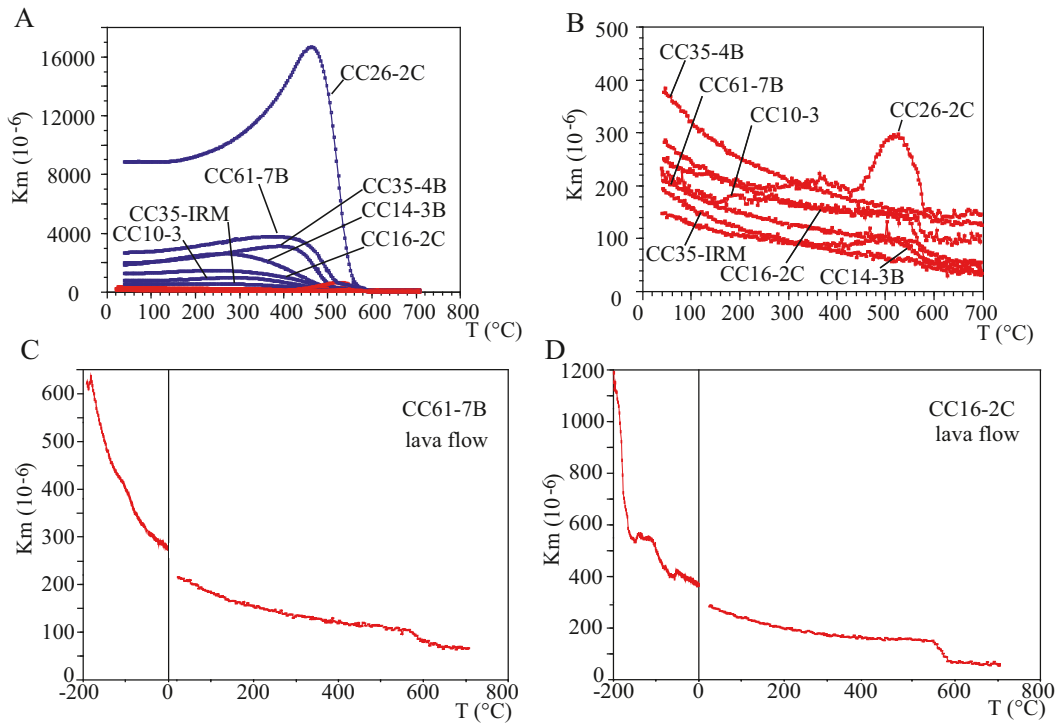


Fig. 2. A) Temperature-dependent susceptibility curves (40 to 700 °C) of heating (in red) and cooling (in blue) for the seven analysed curves, where non-reversibility of curves can be observed. B) Enlargement of the heating curves, where a dominant paramagnetic behaviour can be observed. C) and D) Heating curves (–195 to 700 °C) of two selected samples that show a mixture of paramagnetic and ferromagnetic contributions. Highlight that the break between the low and high temperature dependent susceptibility curves is probably due to the heterogeneities of the sample.

maxima of K_1 are subhorizontal and better grouped than in the non-restored stereoplots in all locations, except for the Cerc and Ansovell sections (Figs. 8 and 9). After bedding correction, the distribution of K_1

shows a dominant WNW-ESE direction in the Argestués, Coll de Vanses and El Ges sections (Fig. 9). In the Cerc section, after bedding restitution, K_1 axes are distributed in two subhorizontal maxima, WNW-ESE and

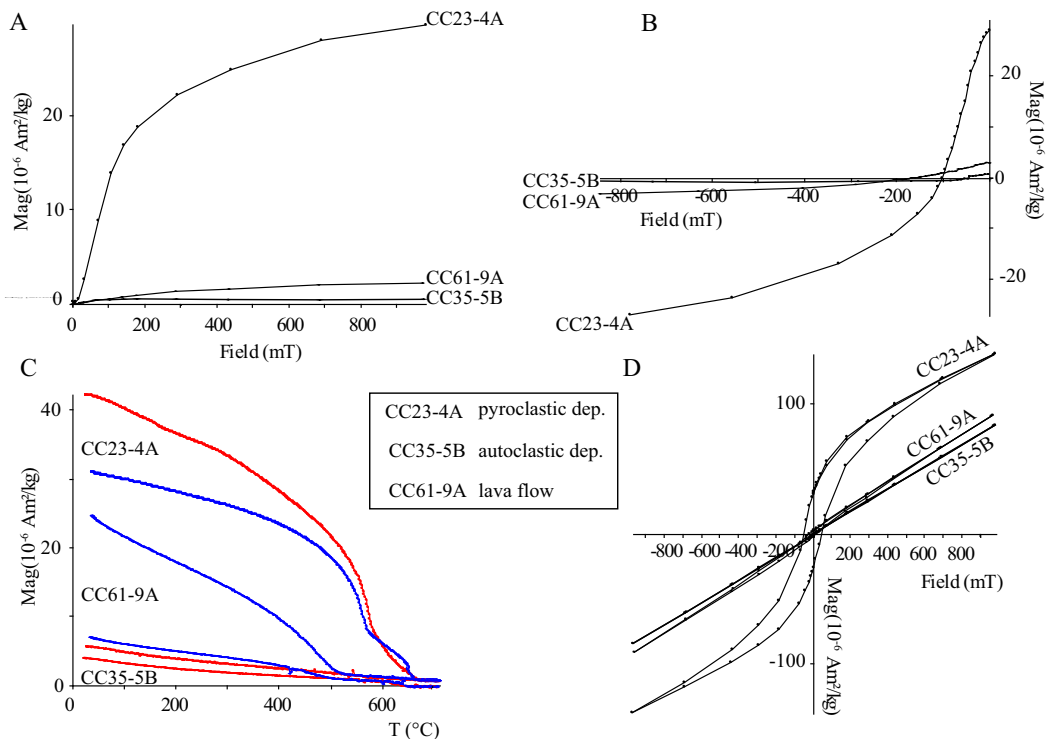


Fig. 3. Magnetic rock study for analysed samples: A) IRM curves. B) Backfield curves. C) Temperature-dependent induced magnetisation curves. D) Hysteresis loops.

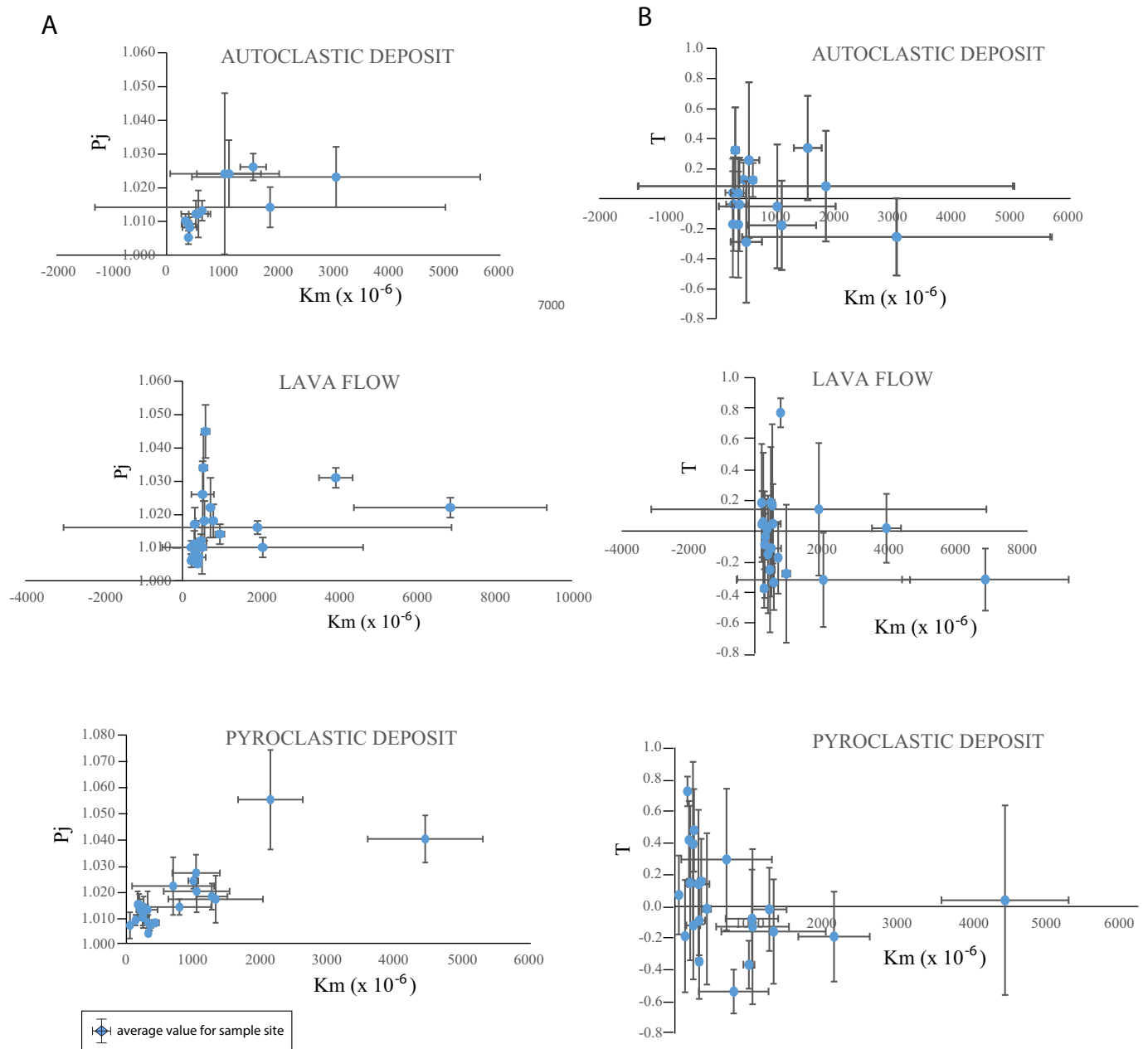


Fig. 4. Diagrams of the magnetic ellipsoid parameters depending on lithological types: A) Corrected anisotropy degree (P_j) versus bulk magnetic susceptibility (K_m). B) Shape parameter (T) versus magnetic susceptibility (K_m). Averaged values from each sampled site.

NNE-SSW, and K_3 axes are subvertical. There are not differences in orientation of K_1 axes related to their stratigraphic position along the transect (Fig. 9). In the Ansovell section, after bedding restitution, K_1 axes show a high directional variability following two maxima around the NW-SE direction and, again, there is not a defined pattern related to their spatial position along the section (Fig. 9). If we consider the whole dataset, an overall pattern showing a dominant WNW-ESE direction for K_1 can be defined (Fig. 9).

4.3. Magnetic fabrics: LT-AMS

The LT-AMS was carried out in five representative sites (Fig. 10) from different lithologies and orientations of the magnetic fabric at room temperature. In the analysed samples, the K_m -LT/ K_m -RT ratio per site ranges between 2.64 and 1.20 indicating the influence of the

ferromagnetic behaviour (Fig. 10B). Nonetheless, sample CC07 (pyroclastic deposit) presents a behaviour close to the pure paramagnetic one. In all the analysed sites, the LT-AMS results overlap the RT-AMS magnetic fabric, and the magnetic parameters P_j and T do not show significant differences (Fig. 10A).

4.4. Microstructural study

The detailed study in thin section of the rocks has allowed: 1) to clearly define the relationship between the petrofabric and the magnetic fabric; 2) to identify the minerals responsible for the petrofabric; and 3) to know the contribution of the tectonic imprint that could potentially modify the original magnetic fabric. Identification of minerals was based upon the habit of crystals, because all the rocks are intensely altered: 1) plagioclases show a partial to total alteration to carbonate;

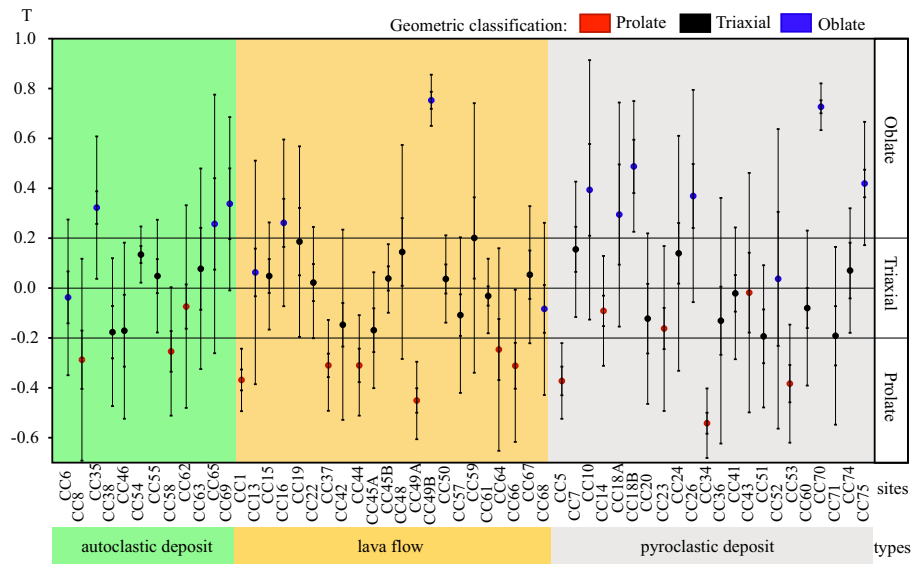


Fig. 5. Type of magnetic ellipsoid per site according to T parameter (whiskers show standard error and standard deviation). In sites where geometry is clearly defined the geometric classification is used. Colors: red (prolate), black (triaxial) and blue (oblate). Explanation in the text.

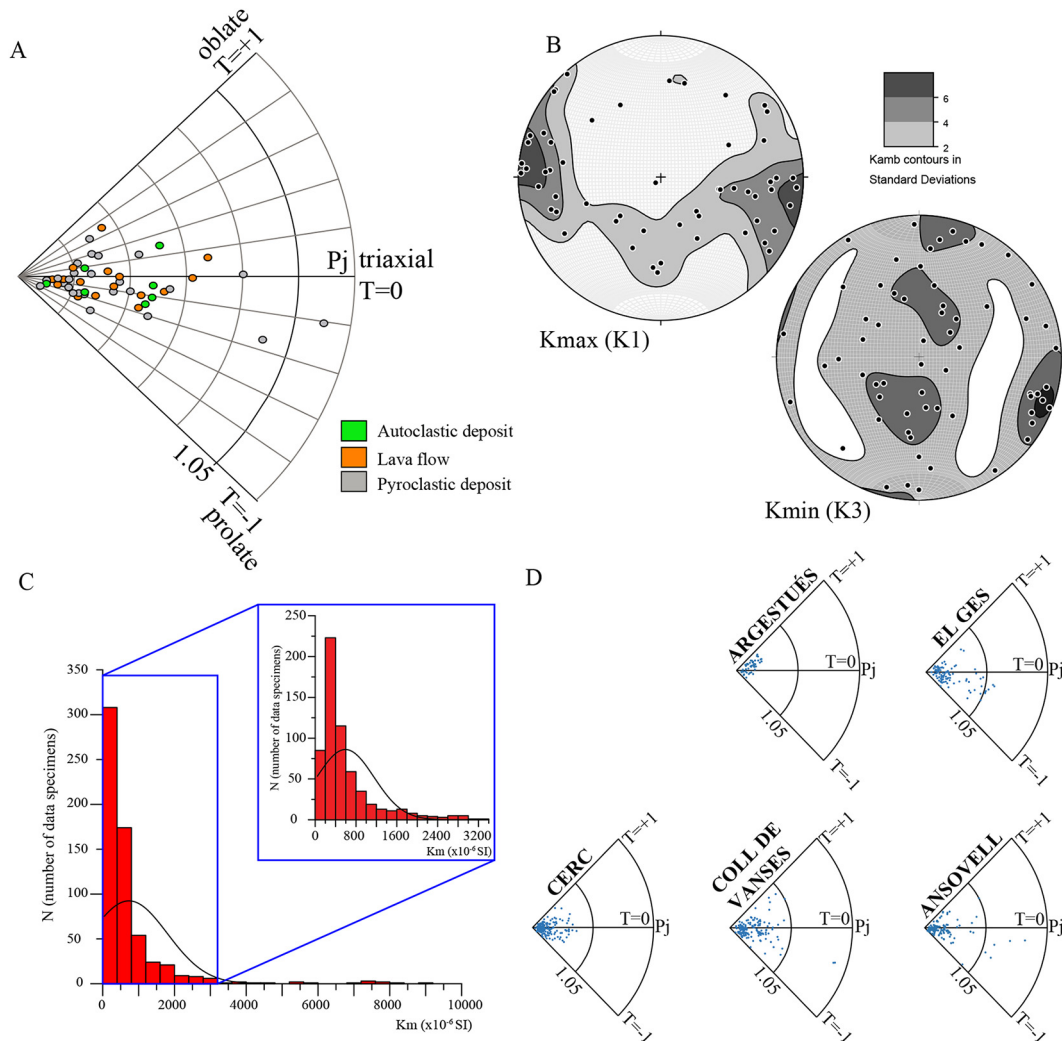


Fig. 6. Polar Pj-T plot (sampling sites means value). B) Density diagrams of magnetic axes, mean value from sampling site, in situ. C) Histogram of mean susceptibilities of the data specimens. D) Polar Pj-T plots (data from specimens from each studied traverses).

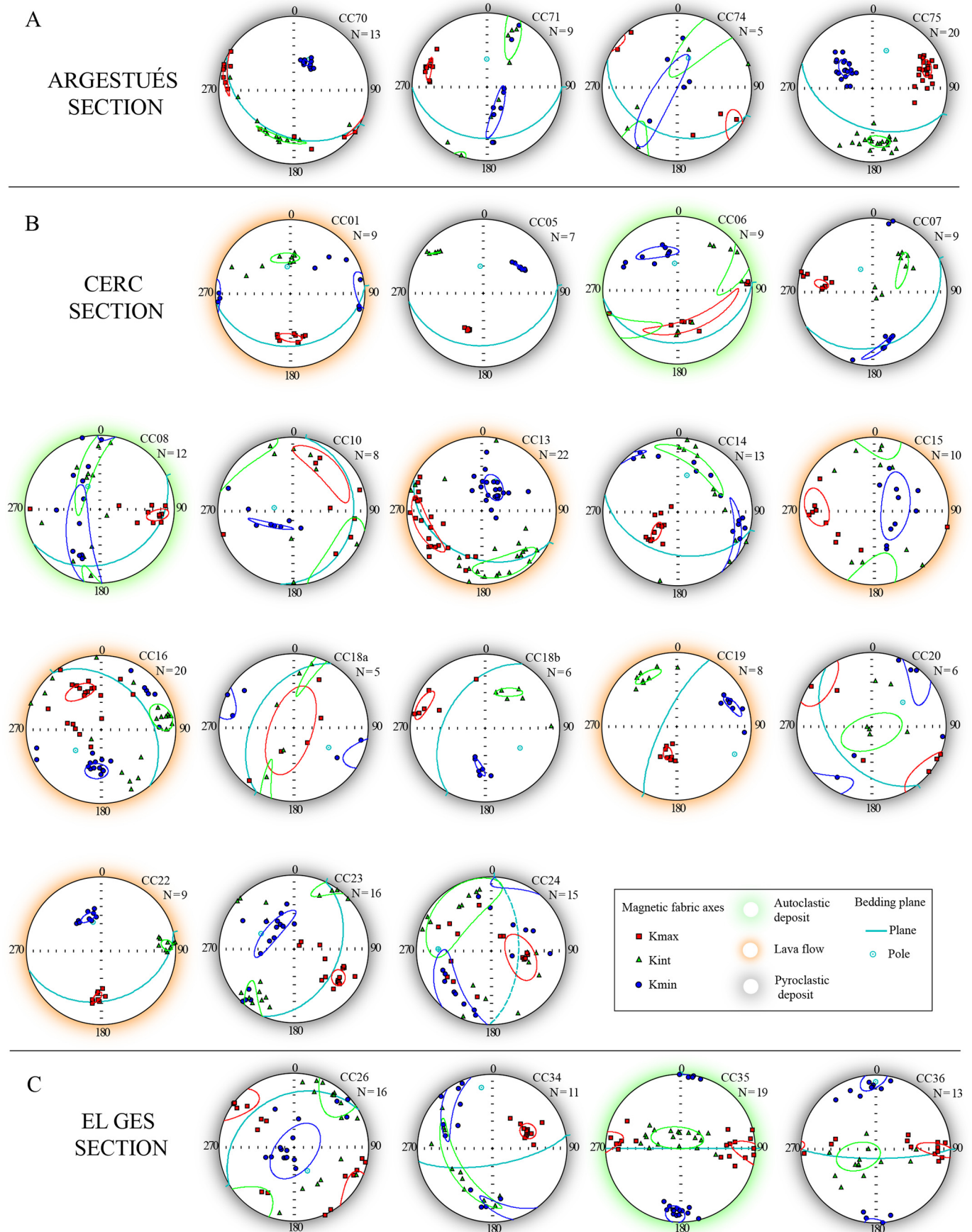


Fig. 7. AMS ellipsoids obtained for each sampling site with 95% confidence ellipses (Jelinek, 1977). The projection of the bedding plane and its pole is represented. A) Argestués section. B) Cerc section. D) Coll de Vanses section. E) Ansovell section.

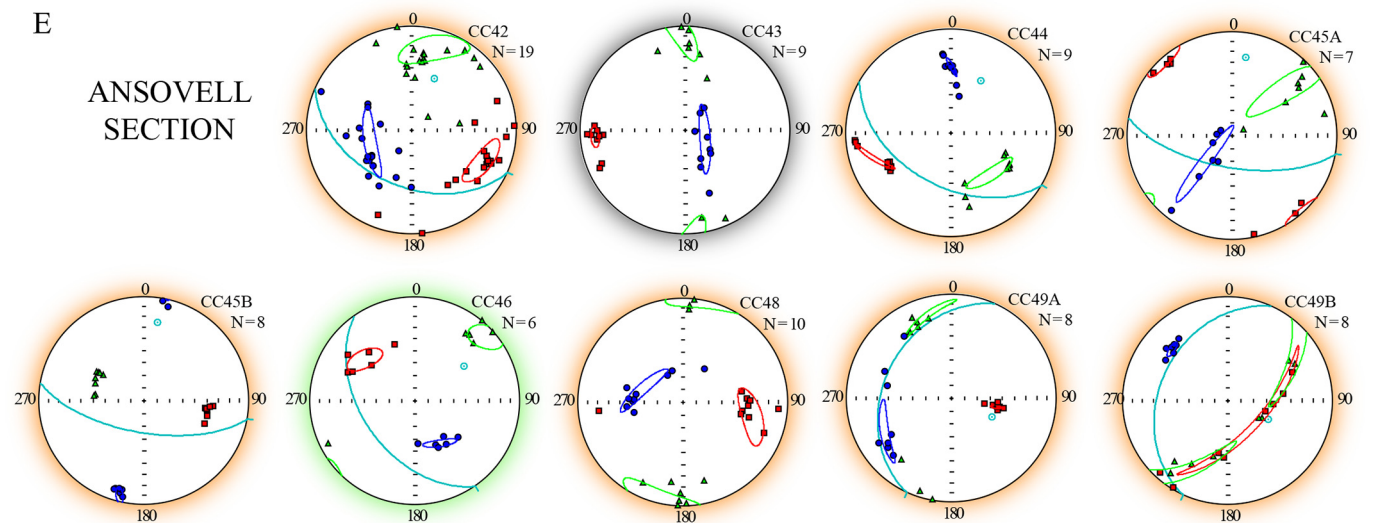
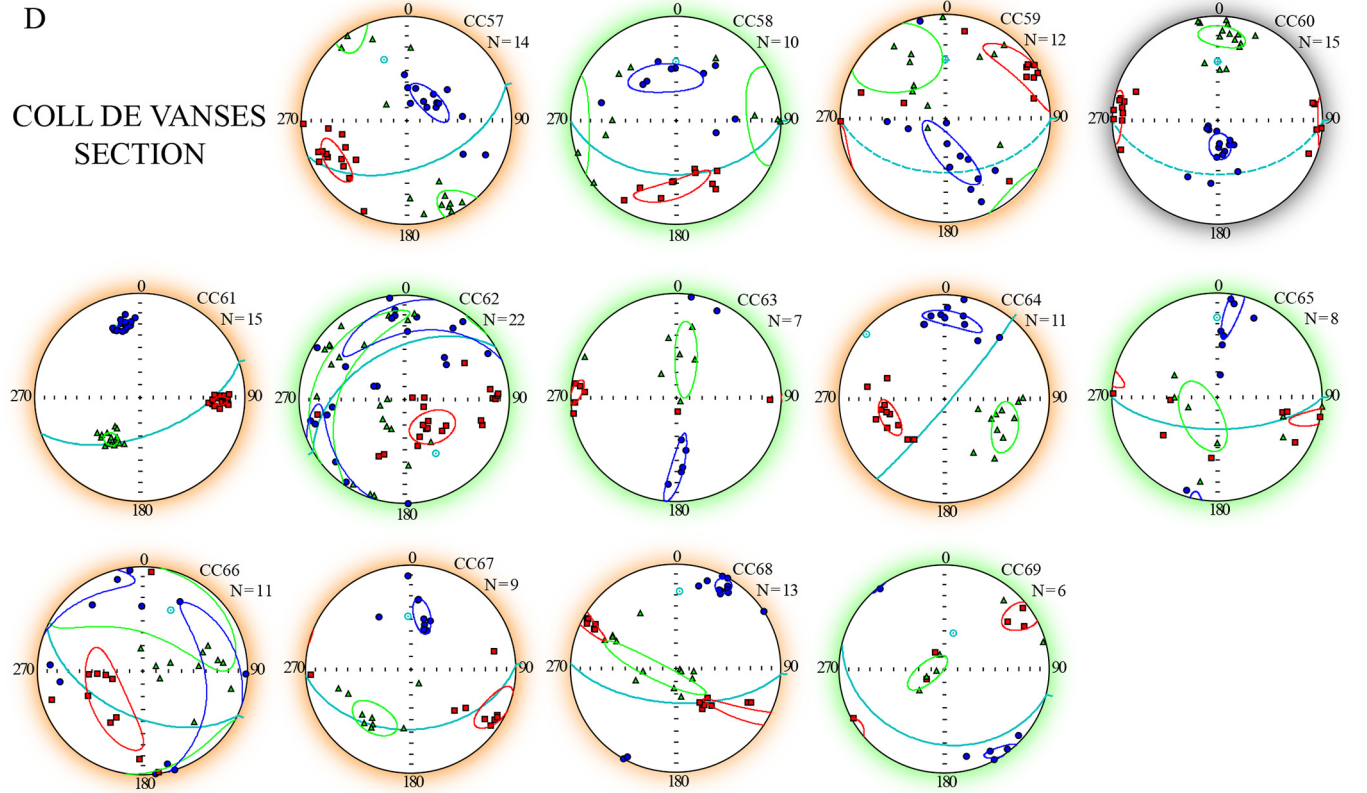
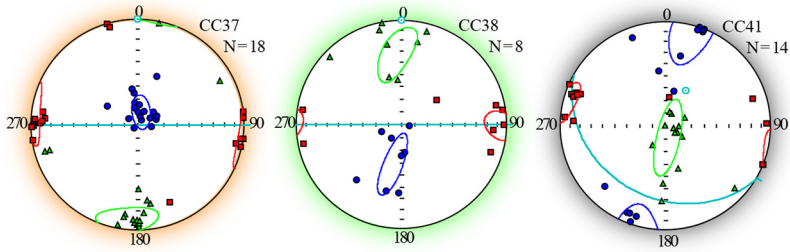


Fig. 7 (continued).

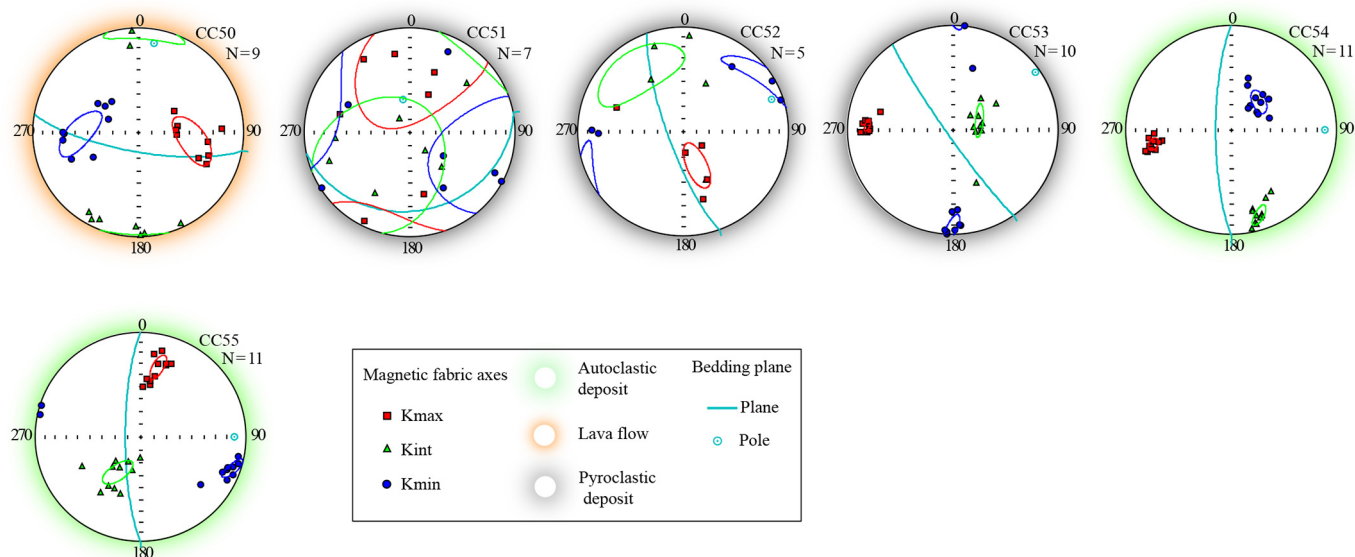


Fig. 7 (continued).

and 2) mafic minerals (amphiboles and pyroxenes) are abundant and totally replaced by phyllosilicates (specially chlorite).

In the samples corresponding to lava flows, plagioclase crystals define the main fabric of the rock (Fig. 11 sample CC48). In some thin sections, the crystals show imbrication or different (even perpendicular) preferred orientations. Furthermore, less abundant, mafic minerals are also aligned with the plagioclases (Fig. 11 sample CC37). Many Fe-oxides are present in the thin sections, distributed randomly and dispersed (Fig. 11 sample CC65) or surrounding the faces of the mafic minerals (Fig. 11 sample CC22). The matrix of the samples usually presents a recrystallization and a partial alteration to carbonate.

In the pyroclastic deposits, ignimbrites are abundant and are characterized by a good orientation of grains, showing elongate, fine-grained juvenile clasts aligned parallel to the flow foliation (Fig. 11 sample CC53). The latter can be defined by concentration of opaque minerals, probably resulting from the early alteration of these rocks.

According to the classification proposed (Fig. 11, see the classification criteria in Subsection 3.6. Microstructural study), 32 sampling sites present an exclusively primary fabric (Type A), 16 sampling sites present a petrofabric with localized, non-pervasive foliation or fracture planes (Type B), seven sampling sites show a tectonic imprint (Type C), that can locally modify the primary fabric, and produce a reorientation of the minerals, and finally, only one sampling site shows a clear tectonic fabric (Type D) with a penetrative foliation that cannot be related to flow.

In thin sections of Type A (Fig. 11), the plagioclase and/or mafic minerals are well aligned. This can be seen, for example, in CC05 (pyroclastic deposit), CC20 (ignimbrite), CC35 (autoclastic deposit), CC49B (lava flow), and CC54 (autoclastic deposit). Even in cases of strong alteration, the orientation of the petrofabric can be identified (e.g. CC14, lava flow). In Type B, the primary fabric is not modified by tectonic features (e.g. CC08, autoclastic deposit, CC52, pyroclastic deposit). Sites CC10 (pyroclastic deposit), and CC58 (autoclastic deposit) are examples of Type C fabrics, where the primary orientation is not modified, in spite of showing more secondary structures. Only one thin section shows a Type D fabric with a penetrative foliation (CC60 pyroclastic deposit) with a tectonic imprint that probably developed under favorable lithological/structural conditions.

5. Discussion and interpretation

5.1. Magnetic properties and magnetic carriers

During the last thirty years it has been demonstrated that AMS is a statistically robust method to characterize the fabrics of deposits of volcanic and volcanoclastic materials such as lava flows and pyroclastic deposits (e.g. Cañón-Tapia and Pinkerton, 2000; Le Pennec et al., 1998; Ort et al., 2015; Porreca et al., 2003). The application of this technique to numerous volcanic deposits around the world has highlighted that the analysis of AMS should be used with caution when determining flow directions because of: (i) problems derived from magnetic mineralogy, that must be carefully checked, (ii) the modification of primary fabrics by subsequent tectonic processes, (iii) the dispersion in the distribution of flow directions, showing interferences that can be compensated by sampling a sufficient number of sites, (iv) the heterogeneity of magnetic fabrics (shape of the ellipsoid at the sample and site scale, etc...) that can be a drawback when interpreting their geometry. Measurements of the magnetic fabrics of lavas and pyroclastic deposits have shown that the characterization of the magnetic carriers to the AMS is needed, especially in rocks yielding high K_m ($\times 10^{-2}$), to avoid an incorrect interpretation of magnetic lineations not related with flow (e.g. Cañón-Tapia, 2004a and references therein; Ort et al., 2015; Pioli et al., 2008; Trippanera et al., 2020). In this work, the mean value of susceptibility for all sites is low when compared with other volcanic rocks in the literature. The mode value obtained is 218×10^{-6} SI, mostly fitting within the paramagnetic domain (Enkin et al., 2020). Conversely to other examples of igneous rocks, K_m values do not show a clear relationship with the considered lithological types, what supports the heterogeneous origin and mineralogical variety of the different volcanic products, to which the diagenetic alteration, with probable crystallization of new phases, is also added. The characterization of the magnetic mineralogy from the thermomagnetic curves indicates that the minerals that define the AMS of the studied rocks are a mixture of phases providing paramagnetic and ferromagnetic (magnetite determined from its T_c of 580 °C and a very minor contribution of haematite) contributions. In any case, the paramagnetic contribution to susceptibility is high in all the lithologies (autoclastic deposits, pyroclastic deposits and lava flows) and allows us to be confident about the matching

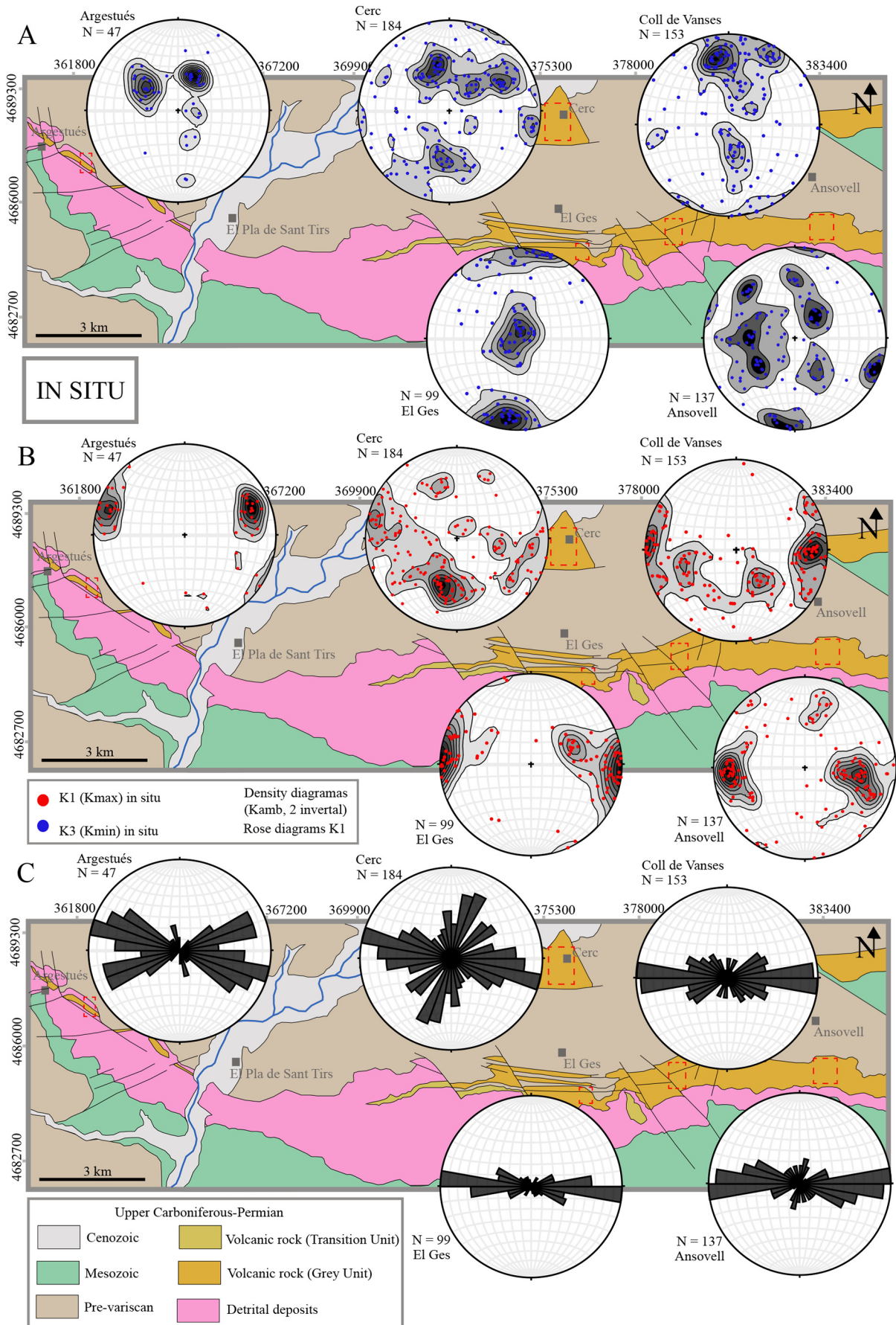


Fig. 8. Density diagrams (Kamb contours, 2% interval) of magnetic axes, data from individual specimens: A) K_3 (Kmin) axes in situ. B) K_1 (Kmax) axes in situ. C) Rose diagrams of K_1 (Kmax) axes in situ.

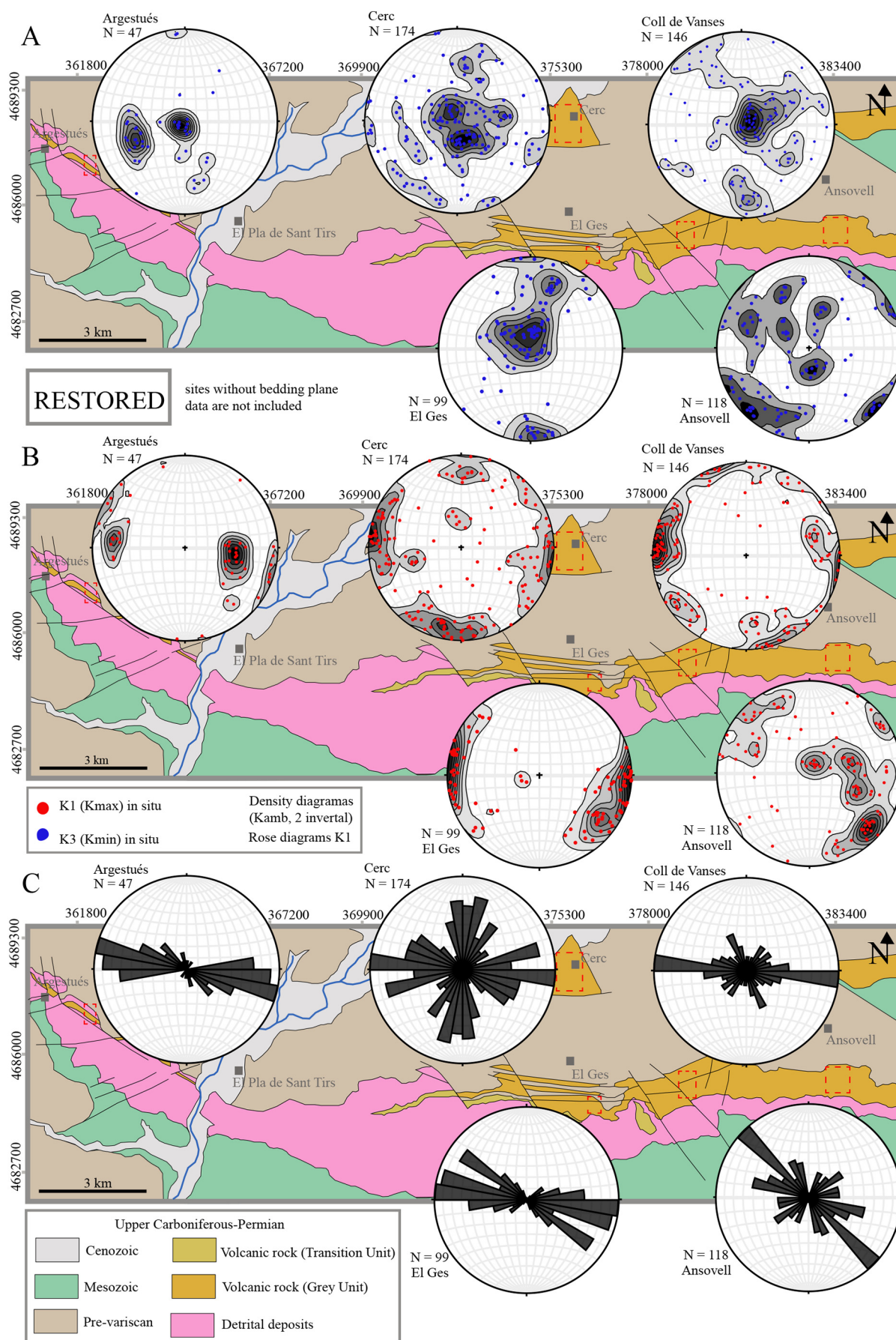


Fig. 9. Density diagrams (Kamb contours, 2% interval) of magnetic axes, data from individual specimens: A) K_3 (K_{min}) axes restored (tilt-corrected). B) K_1 (K_{max}) axes restored. C) Rose diagrams of K_1 (K_{max}) axes restored (tilt-corrected).

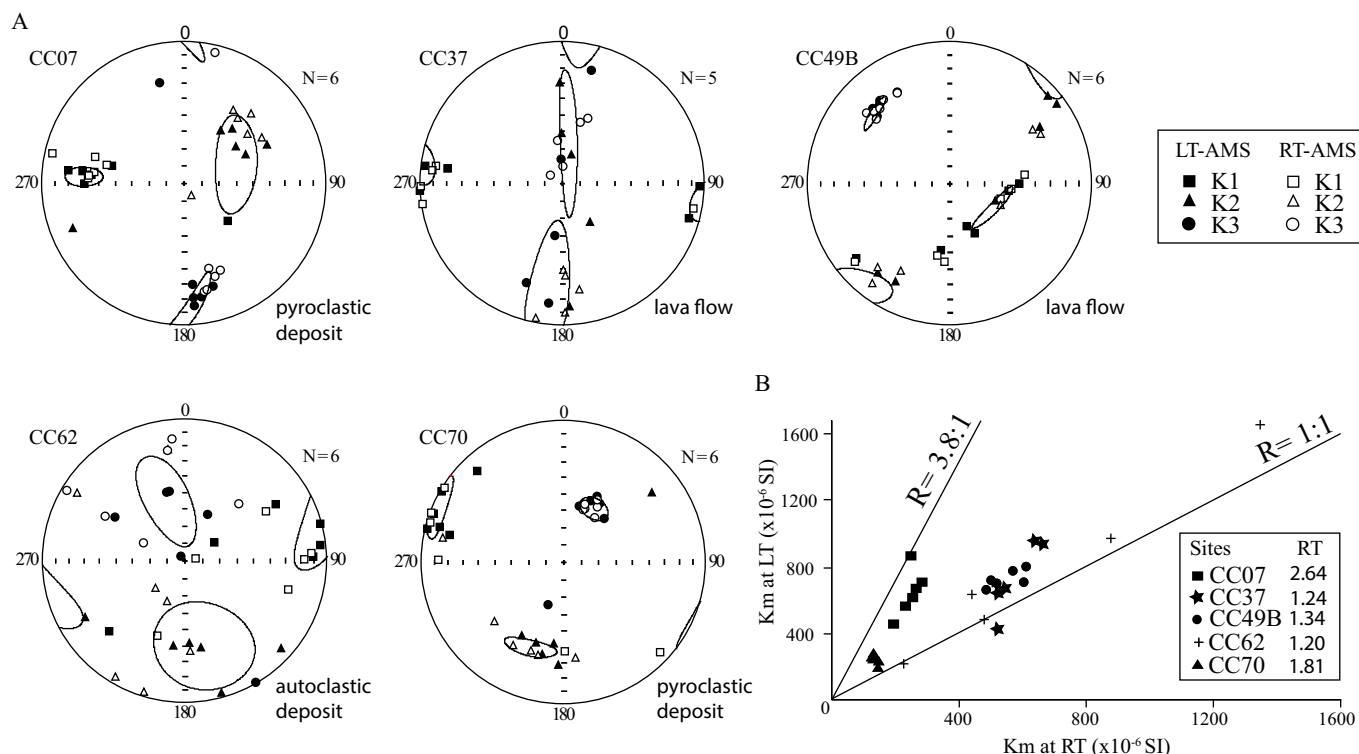


Fig. 10. A) Comparison between RT-AMS (white symbols) and LT-AMS (black symbols) and for RT-AMS, 95% confidence ellipses (Jelinek, 1977) for each sampling site. B) Ratio between the magnetic susceptibility at low and room temperature (LT/RT).

between the mineral preferred orientation and the AMS data. Original paramagnetic minerals (phenocrysts of plagioclase, amphiboles and pyroxenes) are often replaced by other paramagnetic phases such as phyllosilicates and a matrix also containing phyllosilicates). Temperature-dependent susceptibility curves are irreversible (Fig. 2A) evidencing the neoformation of new mineralogical phases (probably magnetite) during heating. Since volcanic rocks are thermally stable, this behaviour can reflect mineralogical alteration and creation of new mineralogical phases after their generation and deposit. This is observed in all lithological types: samples of pyroclastic deposit (CC10–3, CC14–3B and CC26–2C), autoclastic deposit (CC35–4B and CC35–IRM) and lava flow (CC16–2C and CC61–7B). The irreversibility of the curves is also observed in the temperature-dependent magnetization curves, significant in the samples of autoclastic deposit and lava flow (CC35–5B and CC61–9A, respectively) but negligible in the sample of pyroclastic deposit (CC23–4A). Saturation at 100 mT in sample CC35–5B and the no saturation at 1 T in samples CC23–4A and CC61–9A in the isothermal remanent magnetization (IRM) and backfield curves indicates that there are magnetic minerals with low and high coercivity, magnetite and haematite, respectively, in the three analysed lithologies. The wasp-waisted hysteresis can be also related to the presence of different magnetic phases (CC23–4A, Fig. 3D) (Weil and Van der Voo, 2002 and references therein), and the dominance of the paramagnetic contribution is shown by the linear trend of hysteresis loops (CC35–5B and CC61–9A, Fig. 3D). As we have stated, the corrected anisotropy degree P_j is low in all sampled sites, and the parameter T shows triaxial magnetic ellipsoids for most sites, even if we assume a very restricted range for this category (Fig. 5). K_m - P_j and K_m - T diagrams show no correlation between K_m , P_j or T and the sampled lithology (Fig. 4) indicating the neglectable influence of magnetic mineralogy in the AMS. The LT-AMS results indicates the existence of two behaviours, paramagnetic (samples with a significant increase in K_m at low temperature) and ferromagnetic (samples with a lower increase in K_m at low temperature). Remarkably, all the analysed samples show

similar orientations of AMS axes at room and low temperature, what is a good indicator of the reliability of the results.

5.2. Magnetic fabrics and petrofabrics

To check the consistency of data and the relationship between magnetic fabrics and petrofabrics (and also to detect possible magnetic mineralogy artifacts), we compared AMS results with image and petrographic analyses. Our final aim in this case is to verify the reliability of AMS as a paleoflow indicator in the Cadí basin.

The results obtained show that in most samples there is a close relationship between the magnetic fabric and the mineral or grain orientations. In samples CC05 (Fig. 12A) and CC06 (Fig. 12B) a preferred orientation of minerals, mainly plagioclase crystals, in two perpendicular sections, was recognized. This allows to define the plane of the petrographic anisotropy (but not the dominant lineation, that can be qualitatively defined as very close to the direction of one of the sections, according to the shape of grains in the two perpendicular cuts). The plane of the petrographic anisotropy contains the K_1 and the K_2 magnetic anisotropy axes and its pole is located close to K_3 (Fig. 12A and B, respectively). In sample CC05, the magnetic foliation is oblique to the bedding plane measured in field but in sample CC06 both planes are overlapped. In sample CC70 (Fig. 12E), image analysis precludes observing a preferred orientation of particles in any section but graded bedding and alignment of the oxides that constitute the matrix are observed in thin section. The plane defined by oxides, subparallel to the bedding plane measured in the field (Fig. 12E), contains the K_1 and the K_2 axes and its pole is close to K_3 . In sample CC34C, the preferred orientation of mineral grains (mafic minerals) is observed only in one section and shows a subhorizontal ENE–WSW direction, slightly oblique to the E–W trending K_1 axes (Fig. 12C). Finally, sample CC44B shows preferred orientation of plagioclase crystals, observed in polished and thin sections, whose relationship with the magnetic fabric is not straightforward. In any case it should be noted that K_1 axes fall within

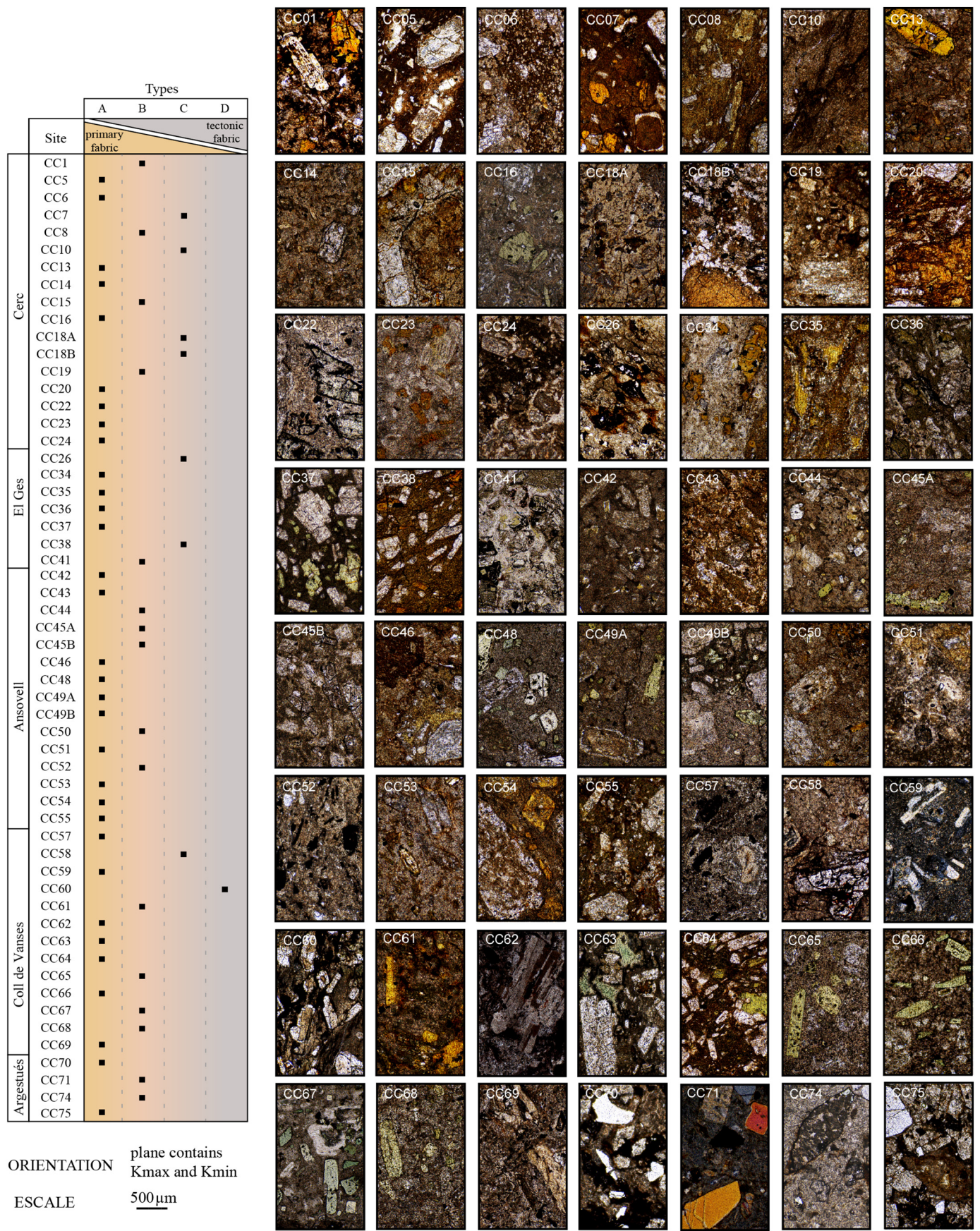
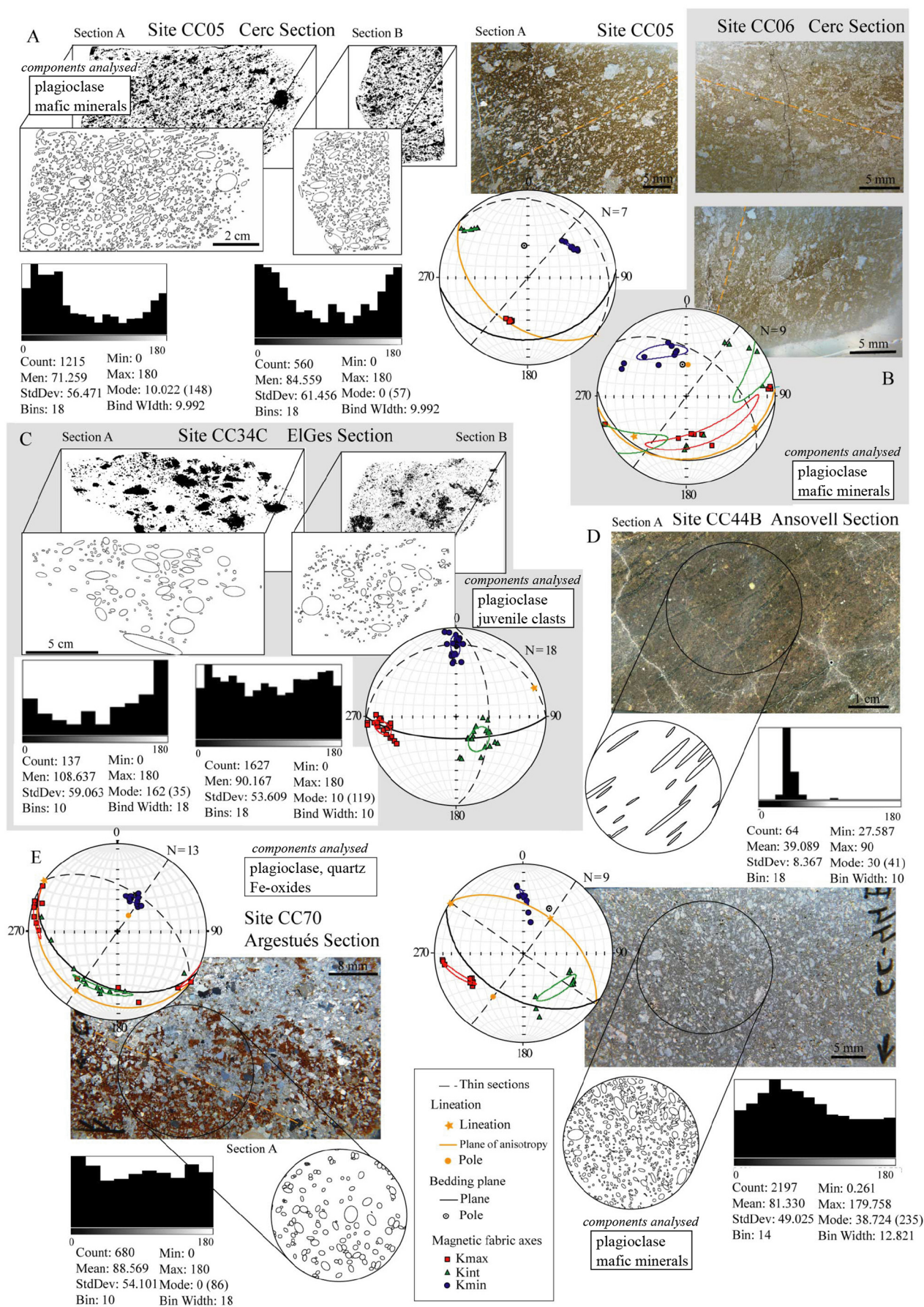


Fig. 11. Results from the microstructural study: classification of the sampling sites according to the contribution of the tectonic imprinting and details of thin sections.



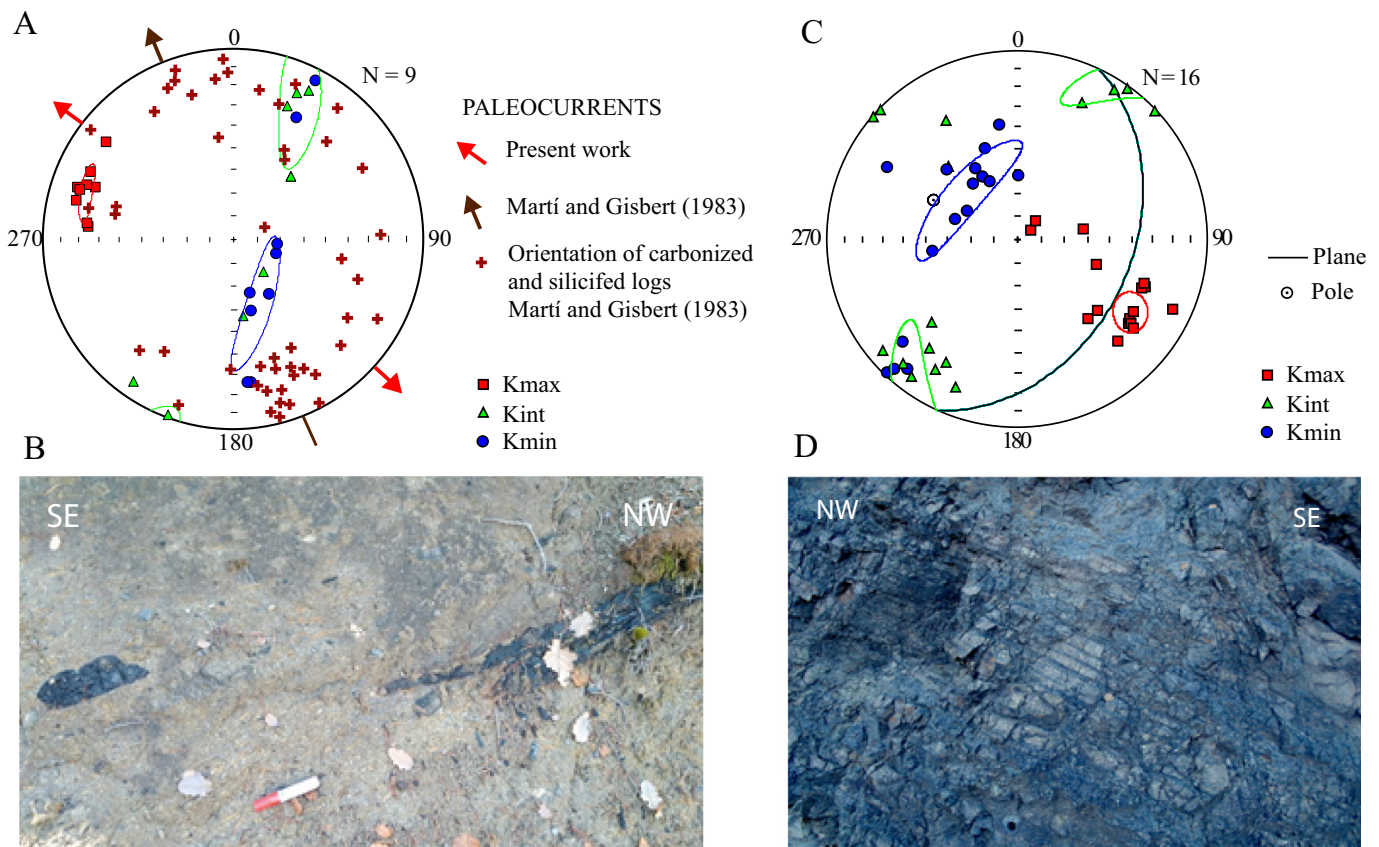


Fig. 13. A) Magnetic fabric (site CC71), paleoflows and orientations of fossil logs. Schmidt net, lower hemisphere stereoplot. B) Carbonized logs from site CC71, Argestués section. C) Magnetic fabric (site CC23), bedding plane and pole of the compositional banding. Schmidt net, lower hemisphere stereoplot. D) Compositional banding from site CC23, Cerc section.

the bedding plane directly measured in the field and K_3 is close to its pole (Fig. 12D).

At outcrop scale, some structures, related to the flow of volcanic and volcanoclastic materials, were recognized, namely oriented fossil tree logs of metric size within a lahar and compositional changes parallel to bedding. In the Argestués section a lahar deposit was described by Gisbert (1981) as an unconsolidated pyroclastic, matrix-supported material including carbonized and silicified logs. In this deposit, the magnetic fabric presents the maximum axes (K_1) clearly clustered in a WNW-ESE direction. This result shows that K_1 is sub-parallel to the paleocurrent inferred from the orientation of logs within the deposit, N130E, carried out for the present work and slightly oblique to data obtained in a previous work (Martí and Gisbert, 1983) (Fig. 13A and B, site CC71) although the detailed interpretation of the outcrop is probably not so straightforward, since the axes of logs are not perfectly contained in the bedding plane, and one of the clusters could be perpendicular to the flow direction.

In the southern zone of the Cerc section, a pyroclastic flow deposit shows a primary compositional banding. In this case, maximum axes (K_1) are clearly clustered within the plane defined by the compositional changes and minimum axes (K_3) are well-grouped perpendicular to its plane. In other sites, where a compositional banding was recognized (CC18, CC24 and CC64); maximum axes (K_1) are within or close to this plane but not as clearly as in site CC23 (Fig. 13C and D).

Therefore, considering these observations, and the consistency observed between magnetic fabrics and flow directions from the systematic thin sections shown in Fig. 12, we can conclude that, for the studied case, the magnetic lineation (i.e. K_1 axes) can be used as a paleoflow indicator.

5.3. Interpretation of paleoflow directions

Together with a detailed description of axes directions, magnetic fabrics were compared according to the Pj and T parameters (Fig. 6). It has not been possible to assign a clear correspondence between the three lithological types and Pj and T values (Fig. 6A). In the same way, our results do not permit to see significant AMS differences based on the different site location across the Cadí basin. In other words, there is a remarkable homogeneity in paleoflow directions both in the horizontal (along strike) and in the vertical (during the time of accumulation of volcanic materials (Fig. 9). Regarding our AMS results, the number and location of volcanic foci are not easy to define. Moreover, the existence of intrusive bodies along the basin axis supports the hypotheses of multiple, aligned vents (see, e.g. Le Corvec et al., 2013; Toprak, 1998, see also discussion about this subject in the next subsection).

The interpretation of AMS data from volcanic and volcanoclastic rocks is not straightforward and several aspects must be taken into account according with previous studies (e.g. Cañón-Tapia, 2004a; Ort

Fig. 12. Image analysis and petrographic study. The following features are shown in each case: fitting particles to ellipses from a binary image by means of ImageJ software; histograms that present the preferred orientation of ellipses according to the angle between its long axis and a horizontal reference line (measured anticlockwise); comparison between the magnetic ellipsoid and the plane of anisotropy (qualitatively defined as very close to the direction of the studied sections). Samples: A) CC05 B) CC06; C) CC34C, D) CC44B and E) CC70. Note that sample CC34C does not correspond to site CC34 but to a sample specifically taken for this analysis.

et al., 2015). For instance, magnetic fabrics in pyroclastic deposits can reflect changes in flow behaviour due to distance from the vent and changes in velocity (Ort et al., 2015). Besides, in lava flows the degree of anisotropy can vary according with the thermal and shearing history of the rock (e.g. Cañón-Tapia and Pinkerton, 2000). Our AMS results show a robust magnetic lineation oriented WNW-ESE (i.e. flow direction) both in situ and corrected (i.e. restoring data to the horizontal) coordinates (Figs. 8, 9). In 15 sites containing 174 specimens, K_3 axes are not close to the vertical after bedding restitution (as expected for a restored primary fabric), conversely to the 41 sites containing 446 specimens that show vertical K_3 . Those 15 sites do not show differences related to mineral carriers and discrepancies between K_3 axes and the poles to bedding could be caused by imprecise measurements of bedding orientation, due to the characteristics of the studied materials, fractures, their complexity and exposure conditions. Nevertheless, the low variation between the orientations of the magnetic lineation (K_1 axes) in situ and restored is also due to the similarity between the strike of bedding and the trend of the lineation. This adds a plus to the reliability in the determination of the trend of the magnetic lineation, that in this way does not rely on the precise determination of bedding in each site. Another question to highlight is that there is not a clear imbrication of K_1 axes (they present a subhorizontal position), as it happens in other examples of volcanic flows (Dedzo et al., 2011; Hillhouse and Wells, 1991; Knight and Walker, 1988; see also Herrero-Bervera et al., 2002). For that reason, it was not possible to define the sense of flow from our data (see next subsection for a discussion on this topic).

5.4. Regional implications for the Late Carboniferous-Permian Cadí basin

The formation of the supercontinent Pangea during the Late Palaeozoic resulted from the collision between Laurussia, Gondwana and also several peri-Gondwana microcontinents (e.g. Avalonia, Armorica, Iberia; Elter et al., 2020; Gutiérrez-Alonso et al., 2008; Padovano et al., 2014). The location of these peri-Gondwana microcontinents between both plates and their irregular boundaries have been postulated to generate coeval transpressional and transtensional tectonics during collision with a complex pattern of shear zones (Arthaud and Matte, 1977; Ballèvre et al., 2018; Dias et al., 2017; Elter et al., 2020; Gutiérrez-Alonso et al., 2004, 2008; Martínez Catalán, 2011; Neubauer and Handler, 2000; Padovano et al., 2011, 2014). During the Late Carboniferous-Permian times, this tectonic scenario in Western and Central Europe, characterized by a major strike-slip component, led to the formation of more than 70 rift basins coeval with a widespread magmatic event involving the extrusion of thick volcanic successions (McCann et al., 2006). In Iberia, two important intracontinental strike-slip shear zones have been identified: the sinistral antithetic Coimbra-Cordoba Shear Zone whose motion occurred before the intrusion of c. 306–303 Ma plutons (Pereira et al., 2010; Pereira et al., 2017) and the dextral Pyrenees Shear Zone (Arche and López-Gómez, 2005; Elter et al., 2020; Grotter et al., 2015). Along the Pyrenean Axial Zone most evidences indicate a general tectonic regime dominated by dextral transpression (e.g. Ábalos et al., 2002; Antolín-Tomás et al., 2009; Druguet et al., 2014; García-Sansegundo, 2004; Gleizes et al., 1998; Leblanc et al., 1996; Román-Berdiel et al., 2004). However, the geodynamic evolution of the Late Palaeozoic-Early Mesozoic small fault-bounded basins from northeastern Iberia is still controversial. One particular feature of these basins is the emplacement of thick volcanic and volcanoclastic rocks interbedded with Late Carboniferous-Permian sediments reflecting a close relationship between tectonism, volcanism and clastic sedimentation (e.g. Gisbert, 1981; Grotter et al., 2015; Lloret et al., 2018; Martí, 1986). The flow pattern obtained from AMS in the volcanic and volcanoclastic rocks of the Cadí basin allows discussing the hypotheses proposed for the origin and evolution of this particular basin, filled with a significant thickness of magma-derived deposits.

In the Cadí basin there is a general agreement on the influence of strike-slip faulting during the Late Carboniferous-Permian (Gisbert, 1981; Speksnijder, 1985; respectively), and both sinistral and dextral displacements have been documented along its major E-W striking faults. Gisbert (1981) underlined the significance of the E-W (N090–085E) to WNW-ESE (N135–140E) and NE-SW (N035E) major fracture systems present in the Late Carboniferous-Permian rocks, but poorly represented in the upper Permian levels and pre-Late Carboniferous Variscan basement. During the Late Carboniferous and Early Permian, some of these fractures had a sinistral transcurrent displacement and were subsequently re-activated during the Pyrenean compression (Late Cretaceous-Miocene, Gisbert, 1981). Speksnijder (1985) proposed that the Cadí basin would have been controlled by an E-W strike-slip fault system with alternate stages of transtension and transpression. This geodynamic scenario would be responsible for the generation of normal faults and grabens and favoured (i) the magma ascent and lava flow emplacement during transtension and (ii) the inversion of normal faults, erosion and generation of unconformities at the basin borders and their corresponding paraconformities at the basin center during transpression. Major faults would reach the base of the crust and the spreading of mainly andesitic lavas would occur through them. A migration of the basin depocenter in space and time towards the east can be inferred from observation of sediment thickness along strike, together with eastward paleocurrent directions along the basin axis (Speksnijder, 1985; Grotter et al., 2015).

Our AMS results provide a clear pattern for the main flow direction, defined by K_1 axes is WNW-ESE direction (in situ and tilt-corrected) and two secondary N-S maxima (slightly NNE-SSW in Cerc section, both in situ and restored) and NE-SW in El Ges, Coll de Vanses and Ansovell sections. In this way, flow directions seem to keep a close relationship with the sets of syn-sedimentary faults described by Gisbert (1981). The main flow direction oriented WNW-ESE is consistent with the geometry of the Cadí basin, compartmented by subvertical fault planes whereby the magma flow was channelized, principally through faults showing N035 and N135–140 direction and not through the main N085–090 set.

Unlike other contexts of inverted sedimentary basins where AMS can be interpreted in terms of extension directions perpendicular to master faults (see e.g. García-Lasanta et al., 2018 and references therein), the results obtained in volcanoclastic rocks in the Cadí basin rather seem to have a stronger imprint inherited from their depositional history (i.e. the initial anisotropy of the petrofabric prevails over their diagenetic/tectonic history). This supports an interpretation relating paleoslopes and magnetic fabrics (e.g. Cañón-Tapia et al., 1996), that, in their turn can be related to tectonic features. Within a basin bounded by E-W to WNW-ESE normal faults, a different set of N-S striking normal faults would create a paleotopography stepped in an E-W direction that would channelize the flow of volcanoclastic products.

Focusing on the origin of the volcanic materials, Martí and Mitjavila (1987) established a model for the Cadí basin in which an initial strike-slip regime gave way to a passive volcanic caldera mechanism. In early stages, the geometry of this basin was conditioned by the late fracturing of the Variscan orogen and the output of magma took place through the faults that delimited basin boundaries. Subsequently, basin subsidence continued because of a progressive pressure loss of the magmatic chamber due to initial eruptions, causing a chamber collapse and the massive extrusion of magma. In this way, this collapse triggered the magma transfer from the subsoil to the surface. Our data can fit with this model, but the particular constancy in the prevailing flow direction, parallel to the basin axis throughout its history, constrains the location of magma chambers, either to (i) the (one or both) longitudinal ends of the basin, out of the study area, where volcanic features are difficult to find or (ii) vents aligned along the basin axis (see e.g. Toramaru, 1988), a hypothesis that integrates also the intrusive features described by Bixel (1984). In this case, the faults perpendicular to the basin axis would provide the large-scale landscape features necessary for the

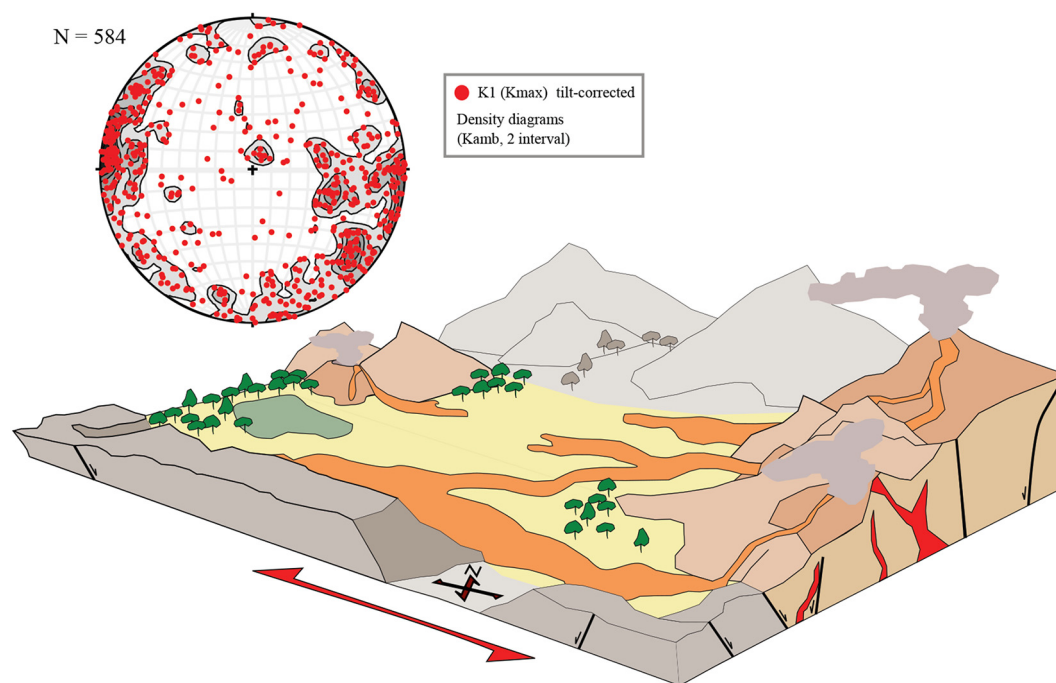


Fig. 14. Interpretation of the Cadí basin during Late Carboniferous-Permian times. Red arrow indicates the direction of lava and volcanoclastic flow obtained from the magnetic study. Only E-W outcrops remains, the rest is unknown (grey colour). Density diagrams (Kamb contours, 2% interval) of K_1 (K_{max}) axes tilt-corrected.

flowing of magma and deposition of pyroclasts along a preferred direction during the period of volcanic activity. For the first hypothesis (end-of-basin foci), if we take into account the migration of the basin depocentre in space and time towards the east (based on sediment thickness variations along strike and paleocurrent directions along the basin axis, [Speksnijder, 1985](#)), it seems reasonable (and due to the absence of other markers) to venture the position of the possible sources of emission of the materials at the western margin of the Cadí basin ([Fig. 14](#)). Nonetheless, [Bixel \(1984\)](#) describes the existence of volcanic calderas and dome structures in the eastern sector of the Cadí basin (eastwards of the studied area). This occurrence, together with the facies transition and the lahar event, distal deposits in the westernmost sector of the basin, rather point to a westwards-directed paleoslope and paleoflow. This hypothesis is more consistent with volcanic features, and can be also compatible with the higher subsidence and depocenter location towards the East, since this movement could be compensated by higher filling rates, controlled by magma ascent and the setting of volcanic buildings (as shown by [Bixel, 1984](#)).

The comparison of results obtained in the Cadí basin in terms of providing the palaeoflow direction with similar data from other southwestern peri-Tethyan, Late Carboniferous-Permian basins can only be done with the Castejón-Laspaules basin ([Izquierdo-Llavall et al., 2013b](#)), where similar results were obtained. The application of this approach in equivalent Late Carboniferous-Permian basins would contribute to understand the interplay between tectonics and volcanism during this stage and to definitively solve the problem of the location of source areas for the Cadí (and other) volcanic basin.

6. Conclusions

Magnetic fabrics in the Cadí basin were acquired during the emplacement and deposition of the volcanoclastic materials and lava flows. The contribution of Cenozoic deformation (N-S compression) to the original, primary fabric is negligible in most samples (as inferred from observations of thin sections). The magnetic lineation (K_1 axes) shows a general trend parallel to the flow direction or within its plane

(equivalent to the bedding plane), what supposes a remarkable applicability of AMS analysis in other ancient deposits of this kind, even if the original mineralogy has been strongly altered, or if the basins have undergone subsequent, compressional deformation stages.

A main WNW-ESE-trending flow pattern is inferred, together with two secondary maxima oriented N-S to slightly NNE-SSW and NE-SW. There are not indicators of the sense of flow, which can only be figured out (from East to West) from regional considerations. Similarly, the number and location of volcanic foci are not easy to define; the existence of (scarce) intrusive bodies or caldera-like structures along the basin axis supports the hypotheses of multiple, aligned vents. The principal WNW-ESE-trending flow pattern points to the N135–140E and N035E sets of fractures as the most relevant in upwelling and distribution of magma within the Cadí basin. The characterization of the interplay between tectonism and volcanism in terms of inferring the main paleoflow directions in the Cadí basin will help to improve our understanding of this particular stage registering the Late Palaeozoic Pangea break-up during the progressive dismantling of the Variscan chain.

Declaration of Competing Interest

The authors declare that they have no known competing financial interests or personal relationships that could have appeared to influence the work reported in this paper.

Acknowledgements

The authors are very grateful to Pablo Calvín and Juanjo Villalaín, from the Department of Physics, University of Burgos, for their help and teachings during laboratory work. The Servicio General de Apoyo a la Investigación-SAI Universidad de Zaragoza carried out the thin sections of samples. This work was supported by projects grants CGL2017-84901-C2-2-P, PID2020-114273GB-C22, PID2019-108753GB-C22 and FPU19/02353 funded by MCIN/AEI/10.13039/501100011033, “ERDF A way of making Europe” and “ESF Investing in your future”. The authors are also grateful to the Associate Editor and to M. Porreca, W. McCarthy

and M.F. Pereira for their thorough revisions of the first version of this manuscript.

References

- Ábalos, B., Carreras, J., Druguet, E., Escuder Viruete, J., Gómez Pugnaire, M.T., Lorenzo Álvarez, S., Quesada, C., Rodríguez-Fernández, R., Gil-Ibarguchi, J.L., 2002. Variscan and pre-Variscan tectonics. In: Gibbons, W., Moreno, T. (Eds.), *The Geology of Spain*. Geological Society, pp. 155–183.
- Aldega, L., Viola, G., Casas-Sainz, A., Marcén, M., Román-Berdiel, T., van der Lelij, R., 2019. Unraveling multiple thermotectonic events accommodated by crustal-scale faults in Northern Iberia, Spain: insights from K-Ar dating of clay Gouges. *Tectonics* 38 (10), 3629–3651.
- Antolín-Tomás, B., Román-Berdiel, T., Casas-Sainz, A., Gil-Peña, I., Oliva, B., Soto, R., 2009. Structural and magnetic fabric study of the Marimán granite (Axial Zone of the Pyrenees). *Int. J. Earth Sci.* 98 (2), 427–441.
- Arche, A., López-Gómez, J., 2005. Sudden changes in fluvial style across the Permian–Triassic boundary in the eastern Iberian Ranges, Spain: Analysis of possible causes. *Palaeogeogr. Palaeoclimatol. Palaeoecol.* 229 (1–2), 104–126.
- Arthaud, F., Matte, P., 1977. Late Paleozoic strike-slip faulting in southern Europe and northern Africa: result of a right-lateral shear zone between the Appalachians and the Urals. *Geol. Soc. Am. Bull.* 88 (9), 1305–1320.
- Ballèvre, M., Manzotti, P., Dal Piaz, G.V., 2018. Pre-Alpine (Variscan) inheritance: a key for the location of the future Valais Basin (Western Alps). *Tectonics* 37 (3), 786–817.
- Barnolas, A., Pujalte, V., 2004. La Cordillera Pirenaica: Definición, límites y división. In: Vera, J.A. (Ed.), *Geología de España*. SGE-IGME, Madrid, pp. 233–241.
- Bixel, F., 1984. *Le Volcanisme Stéphano-Permien des Pyrénées*. Thèse d'Etat Université de Toulouse, p. 639.
- Bixel, F., Lucas, C.L., 1983. Magmatisme, tectonique et sédimentation dans les fossés stéphano-permiens des Pyrénées occidentales. *Rev. Géol. Dynam. Géol. Phys.* 24 (4), 329–342.
- Borradaile, G.J., Jackson, M., 2004. Anisotropy of magnetic susceptibility (AMS): Magnetic petrofabrics of deformed rocks. Geological Society Special Publication <https://doi.org/10.1144/GSL.SP.2004.238.01.18>.
- Bullock, L.A., Gertisser, R., O'driscoll, B., 2018. Emplacement of the Rocche Rosse rhyolite lava flow (Lipari, Aeolian Islands). *Bull. Volcanol.* 80 (5), 1–19.
- Burg, J.P., Brun, J.P., Van Den Driessche, J., 1990. Le sillon houiller du Massif Central français: faille de transfert pendant l'amincissement crustal de la chaîne. *Comptes rendus de l'Académie des sciences. Série 2, Mécanique, Physique, Chimie, Sciences de l'Univers, Sciences de la Terre* 311 (1), 147–152.
- Burg, J.P., Van den Driessche, J., Brun, J.P., 1994. Syn-to post-thickening extension in the Variscan Belt of Western Europe: modes and structural consequences. *Bull. Soc. Géol. France* 3, 33–51.
- Cagnoli, B., Tarling, D.H., 1997. The reliability of anisotropy of magnetic susceptibility (AMS) data as flow direction indicators in friable base surge and ignimbrite deposits: Italian examples. *J. Volcanol. Geotherm. Res.* 75 (3–4), 309–320.
- Calvín, P., Casas, A.M., Villalán, J.J., Tierz, P., 2014. Reverse magnetic anomaly controlled by Permian Igneous rocks in the Iberian Chain (N Spain). *Geol. Acta* 12 (3), 0193–0207.
- Cañón-Tapia, E., 2004a. Anisotropy of magnetic susceptibility of lava flows and dykes: a historical account. *Geol. Soc. Lond., Spec. Publ.* 238 (1), 205–225.
- Cañón-Tapia, E., 2004b. Flow direction and magnetic mineralogy of lava flows from the central parts of the Peninsula of Baja California, Mexico. *Bull. Volcanol.* 66 (5), 431–442.
- Cañón-Tapia, E., Pinkerton, H., 2000. The anisotropy of magnetic susceptibility of lava flows: an experimental approach. *J. Volcanol. Geotherm. Res.* 98 (1–4), 219–233.
- Cañón-Tapia, E., Walker, G.P., Herrero-Bervera, E., 1995. Magnetic fabric and flow direction in basaltic pahoehoe lava of Xitle volcano, Mexico. *J. Volcanol. Geotherm. Res.* 65 (3–4), 249–263.
- Cañón-Tapia, E., Walker, G.P., Herrero-Bervera, E., 1996. The internal structure of lava flows—insights from AMS measurements I: near-vent a'a. *J. Volcanol. Geotherm. Res.* 70 (1–2), 21–36.
- Capote, R., Muñoz, J.A., Simon, J.L., Liesa, C.L., Arlegui, L.E., 2002. In: Gibbons, W., y Moreno M.T. (Eds.), *Alpine Tectonics 1: The Alpine System North of the Betic Cordillera*. En: *Geology of Spain*. Geological Society of London, London, pp. 367–400.
- Cas, R.A., Wright, H.M., Folkes, C.B., Lesti, C., Porreca, M., Giordano, G., Viramonte, J.G., 2011. The flow dynamics of an extremely large volume pyroclastic flow, the 2.08-Ma Cerro Galán Ignimbrite, NW Argentina, and comparison with other flow types. *Bull. Volcanol.* 73 (10), 1583–1609.
- Chadima, M., Hrouda, F., 2012. *Cureval 8.0: Thermomagnetic Curve Browser for Windows*. Agico, Inc.
- Chadima, M., Jelínek, V., 2019. *Anisof5.1.03: Anisotropy Data Browser for Windows*. Agico, Inc.
- Coward, M.P., 1980. The analysis of flow profiles in a basaltic dyke using strained vesicles. *J. Geol. Soc.* 137 (5), 605–615.
- Dedzo, M.G., Nédélec, A., Nono, A., Njanko, T., Font, E., Kamgang, P., Njonfang, E., Launeau, P., 2011. Magnetic fabrics of the Miocene ignimbrites from West-Cameroon: implications for pyroclastic flow source and sedimentation. *J. Volcanol. Geotherm. Res.* 203 (3–4), 113–132.
- Dias, R., Moreira, N., Ribeiro, A., Basile, C., 2017. Late Variscan deformation in the Iberian Peninsula; a late feature in the Laurentia–Gondwana dextral collision. *Int. J. Earth Sci.* 106 (2), 549–567.
- Druguet, E., Castro, A., Chichorro, M., Pereira, M.F., Fernández, C., 2014. Zircon geochronology of intrusive rocks from Cap de Creus, Eastern Pyrenees. *Geol. Mag.* 151 (6), 1095–1114.
- Ellwood, B.B., 1978. Flow and emplacement direction determined for selected basaltic bodies using magnetic susceptibility anisotropy measurements. *Earth Planet. Sci. Lett.* 41 (3), 254–264.
- Elter, F.M., Gaggero, L., Mantovani, F., Pandeli, E., Costamagna, L.G., 2020. The Atlas-East Variscan-Elbe shear system and its role in the formation of the pull-apart Late Palaeozoic basins. *Int. J. Earth Sci.* 109, 739–760.
- Enkin, R.J., Hamilton, T.S., Morris, W.A., 2020. The Henkel petrophysical plot: mineralogy and lithology from physical properties. *Geochem. Geophys. Geosyst.* 21 (1) e2019GC008818.
- Faure, M., Monié, P., Pin, C., Maluski, H., Leloix, C., 2002. Late Visean thermal event in the northern part of the French Massif Central: new 40 Ar/39 Ar and Rb–Sr isotopic constraints on the Hercynian syn-orogenic extension. *Int. J. Earth Sci.* 91 (1), 53–75.
- Franke, W., 2000. The mid-European segment of the Variscides: tectonostratigraphic units, terrane boundaries and plate tectonic evolution. *Geol. Soc. Lond., Spec. Publ.* 179 (1), 35–61.
- García-Lasanta, C., Oliva-Urcia, B., Casas-Sainz, A.M., Román-Berdiel, T., Izquierdo-Llavall, E., Soto, R., Calvín, P., El Moussaid, B., Ouardi, H., Kullberg, J.C., Villalán, J.J., 2018. Inversion tectonics and magnetic fabrics in Mesozoic basins of the Western Tethys: a review. *Tectonophysics* 745, 1–23.
- García-Sansegundo, J., 2004. Estructura varisca de los Pirineos. In: Vera, J.A. (Ed.), *Geología de España*. SGE-IGME, Madrid, pp. 254–258.
- Gisbert, J., 1981. Estudio Geológico – Petroológico del Estefaniense – Pérmico de la Sierra del Cadi (Pirineo de Lérida). *Diagenesis y Sedimentología*. Unpublished PhDUniversity of Zaragoza, p. 472.
- Gleizes, G., Leblanc, D., Santana, V., Olivier, P., Bouchez, J.L., 1998. Sigmoidal structures featuring dextral shear during emplacement of the Hercynian granite complex of Cauterets–Panticosa (Pyrenees). *J. Struct. Geol.* 20 (9–10), 1229–1245.
- Gretter, N., Ronchi, A., López-Gómez, J.L., Arche, A., De la Horra, R., Barrenechea, J., Lago, M., 2015. The Late Paleozoic–Early Mesozoic from the Catalan Pyrenees (Spain): 60 Myr of environmental evolution in the frame of the western peri-Tethyan palaeogeography. *Earth Sci. Rev.* 150, 2–26. <https://doi.org/10.1016/j.earscirev.2015.09.001>.
- Gutiérrez-Alonso, G., Fernandez-Suarez, J., Weil, A.B., 2004. Orocline triggered lithospheric delamination. *Geol. Soc. Am.* 383, 121–130.
- Gutiérrez-Alonso, G., Fernandez-Suarez, J., Weil, A.B., Murphy, J.B., Nance, R.D., Corfu, F., Johnston, S.T., 2008. Self-subduction of the Pangaea global plate. *Nat. Geosci.* 1, 549–553. <https://doi.org/10.1038/ngeo250>.
- Gutiérrez-Alonso, G., Fernández-Suárez, J., Jeffries, T.E., Johnston, S.T., Pastor-Galán, D., Murphy, J.B., Franco, P., Gonzalo, J.C., 2011. Diachronous post-orogenic magmatism within a developing orocline in Iberia, European Variscides. *Tectonics* 30 (5).
- He, B., Xu, Y.G., Huang, X.L., Luo, Z.Y., Shi, Y.R., Yang, Q.J., Yu, S.Y., 2007. Age and duration of the Emeishan flood volcanism, SW China: geochemistry and SHRIMP zircon U–Pb dating of silicic ignimbrites, post-volcanic Xuanwei Formation and clay tuff at the Chaotian section. *Earth Planet. Sci. Lett.* 255 (3–4), 306–323.
- Herrero-Bervera, E., Cañón-Tapia, E., Walker, G.P., Tanaka, H., 2002. Magnetic fabrics study and inferred flow directions of lavas of the Old Pali Road, O'ahu, Hawaii. *J. Volcanol. Geotherm. Res.* 118 (1–2), 161–171.
- Hillhouse, J.W., Wells, R.E., 1991. Magnetic fabric, flow directions, and source area of the lower Miocene Peach Springs Tuff in Arizona, California, and Nevada. *J. Geophys. Res. Solid Earth* 96 (B7), 12443–12460.
- Hrouda, F., 1994. A technique for the measurement of thermal changes of magnetic susceptibility of weakly magnetic rocks by the CS-2 apparatus and KLY-2 Kappabridge. *Geophys. J. Int.* 118 (3), 604–612.
- Hrouda, F., Jelínek, V., Zapletal, K., 1997. Refined technique for susceptibility resolution into ferromagnetic and paramagnetic components based on susceptibility temperature-variation measurement. *Geophys. J. Int.* 129 (3), 715–719.
- Ihmlé, P.F., Hirt, A.M., Lowrie, W., Dietrich, D., 1989. Inverse magnetic fabric in deformed limestones of the Morcles Nappe, Switzerland. *Geophys. Res. Lett.* 16 (12), 1383–1386.
- Incoronato, A., Addison, F.T., Tarling, D.H., Nardi, G., Pescatore, T., 1983. Magnetic fabric investigations of pyroclastic deposits from Phlegrean Fields, southern Italy. *Nature* 306 (5942), 461–463.
- Issachar, R., Levi, T., Lyakhovsky, V., Marco, S., Weinberger, R., 2016. Improving the method of low-temperature anisotropy of magnetic susceptibility (LT-AMS) measurements in air. *Geochem. Geophys. Geosyst.* 17 (7), 2940–2950.
- Izquierdo-Llavall, E., Aldega, L., Cantarelli, V., Corrado, S., Gil-Peña, I., Invernizzi, C., Casas, A.M., 2013a. On the origin of cleavage in the Central Pyrenees: structural and paleothermal study. *Tectonophysics* 608, 303–318.
- Izquierdo-Llavall, E., Casas-Sainz, A., Oliva-Urcia, B., Scholger, R., 2013b. Palaeomagnetism and magnetic fabrics of the Late Palaeozoic volcanism in the Castejón-Laspaules basin (Central Pyrenees). Implications for palaeoflow directions and basin configuration. *Geol. Mag.* 151 (5), 777–797.
- Jelínek, V., 1977. *The Statistical Theory of Measuring Anisotropy of Magnetic Susceptibility of Rocks and its Application*. Geofyzika, Brno.
- Jelínek, V., 1981. Characterization of the magnetic fabric of rocks. *Tectonophysics* 79, 63–70.
- Jerram, D.A., Svensen, H.H., Planke, S., Polozov, A.G., Torsvik, T.H., 2016. The onset of flood volcanism in the north-western part of the Siberian Traps: explosive volcanism versus effusive lava flows. *Palaeogeogr. Palaeoclimatol. Palaeoecol.* 441, 38–50.
- Johnston, S.T., Weil, A.B., Gutiérrez-Alonso, G., 2013. Oroclines: thick and thin. *Geol. Soc. Am. Bull.* 125 (5–6), 643–663.
- Knight, M.D., Walker, G.P., 1988. Magma flow directions in dikes of the Koolau Complex, Oahu, determined from magnetic fabric studies. *J. Geophys. Res. Solid Earth* 93 (B5), 4301–4319.
- Knight, M.D., Walker, G.P., Ellwood, B.B., Diehl, J.F., 1986. Stratigraphy, paleomagnetism, and magnetic fabric of the Toba Tuffs: constraints on the sources and eruptive styles. *J. Geophys. Res. Solid Earth* 91 (B10), 10355–10382.

- Lago, M., Arranz, E., Pocoví, A., Galé, C., Gil-Imaz, A., 2004. Lower Permian magmatism of the Iberian Chain, Central Spain, and its relationship to extensional tectonics. *Geol. Soc. Lond., Spec. Publ.* 223 (1), 465–490.
- Lago, M., Gil, A., Arranz, E., Galé, C., Pocoví, A., 2005. Magmatism in the intracratonic Central Iberian basins during the Permian: palaeoenvironmental consequences. *Palaeogeogr. Palaeoclimatol. Palaeoecol.* 229 (1–2), 83–103.
- Le Corvec, N., Spörli, K.B., Rowland, J., Lindsay, J., 2013. Spatial distribution and alignments of volcanic centers: clues to the formation of monogenetic volcanic fields. *Earth Sci. Rev.* 124, 96–114.
- Le Pennec, J.L., Chen, Y., Diot, H., Froger, J.L., Gourgaud, A., 1998. Interpretation of anisotropy of magnetic susceptibility fabric of ignimbrites in terms of kinematic and sedimentological mechanisms: an Anatolian case-study. *Earth Planet. Sci. Lett.* 157 (1–2), 105–127.
- Leblanc, D., Gleizes, G., Roux, L., Bouchez, J.L., 1996. Variscan dextral transpression in the French Pyrenees: new data from the Pic des Trois-Seigneurs granodiorite and its country rocks. *Tectonophysics* 261 (4), 331–345.
- Leonhardt, R., 2006. Analyzing rock magnetic measurements: the RockMagAnalyzer 1.0 software. *Comput. Geosci.* 32 (9), 1420–1431.
- Lloret, J., Ronchi, A., López-Gómez, J., Grotter, N., De la Horra, R., Barrenechea, J.F., Arche, A., 2018. Syn-tectonic sedimentary evolution of the continental late Palaeozoic-early Mesozoic Erill Castell-Estac Basin and its significance in the development of the Central Pyrenees Basin. *Sediment. Geol.* 374, 134–157.
- MacDonald, W.D., Palmer, H.C., Deino, A.L., Shen, P.-Y., 2012. Insights into deposition and deformation of intra-caldera ignimbrites, Central Nevada. *J. Volcanol. Geotherm. Res.* 245–246, 40–54.
- Martí, J., 1986. *El Volcanisme Explosiu Tardihercinià del Pirineu Català*. PhD Thesis Universitat de Barcelona 304 p.
- Martí, J., Gisbert, P., 1983. Secuencias ignimbriticas y lahares calientes en el estefano-autuniense del Pirineo Catalán. Congreso Internacional de Estratigrafía y Geología del Carbonífero 10. Resúmenes.
- Martí, J., Mitjavila, J., 1987. Calderas volcánicas pasivas: un ejemplo en el Estefaniense del Pirineo Catalán. *Geogaceta* 2, 19–22.
- Martí, J., Mitjavila, J., 1988. El volcanismo tardihercínico del Pirineo Catalán, II: caracterización de la actividad explosiva. *Acta Geol. Hisp.* 23 (1), 21–31.
- Martínez Catalán, J.R., 2011. Are the oroclines of the Variscan belt related to late Variscan strike-slip tectonics? *Terra Nova* 23 (4), 241–247.
- Mattauer, M., 1968. Les traits structuraux essentiels de la chaîne pyrénéenne. *Revue de Géologie Dynamique et de Géographie Physique*, 2è sér. 10 (1), 3–12.
- McCann, T., Pascal, C., Timmerman, M.J., Krzywiec, P., López-Gómez, J., Wetzel, L., Krawczyk, C.M., Rieke, H., Lamarche, J., 2006. Post-Variscan (end Carboniferous–Early Permian) basin evolution in western and central Europe. *Geol. Soc. Lond. Mem.* 32 (1), 355–388.
- Mey, J.F.W., Nagtegaal, P.J.C., Roberti, K.J., Hartevelt, J.J.A., 1968. Lithostratigraphic subdivision of post-Hercynian deposits in the south-central Pyrenees, Spain. *Leidse. Geol. Meded.* 41 (1), 221–228.
- Mujal, E., Grotter, N., Ronchi, A., López-Gómez, J., Falconnet, J., Diez, J.B., De la Horra, R., Bolet, A., Oms, O., Arche, A., Barrenechea, J., Steyer, J.S., Fortuny, J., 2016. Constraining the Permian/Triassic transition in continental environments: stratigraphic and paleontological record from the Catalan Pyrenees (NE Iberian Peninsula). *Palaeogeogr. Palaeoclimatol. Palaeoecol.* 445, 18–37.
- Muñoz, J.A., 1992. Evolution of a continental collision belt: ECORS-Pyrenees crustal balanced cross-section. *Thrust Tectonics*. Springer, Dordrecht, pp. 235–246.
- Muñoz, J.A., 2019. Alpine Orogeny: Deformation and Structure in the Northern Iberian Margin (Pyrenees sl). In *The Geology of Iberia: A Geodynamic Approach*. Springer, pp. 433–451.
- Murphy, J.B., Nance, R.D., Cawood, P.A., 2009. Contrasting modes of supercontinent formation and the conundrum of Pangea. *Gondwana Res.* 15 (3–4), 408–420.
- Nagtegaal, P.J., 1969. Sedimentology, paleoclimatology, and diagenesis of post-Hercynian continental deposits in the south-Central Pyrenees, Spain. *Leidse. Geol. Meded.* 42 (1), 143–238.
- Neubauer, F., Handler, R., 2000. Variscan orogeny in the Eastern Alps and Bohemian Massif: how do these units correlate? *Mitteilungen der Österreichischen Geologischen Gesellschaft* 92, 35–59.
- Nye, J.F., 1957. *The Physical Properties of Crystals: Their Representation by Tensors and Matrices*. Clarendon Press, Oxford, p. 333.
- Oliva-Urcia, B., Larrasoña, J.C., Pueyo, E.L., Gil-Imaz, A., Mata, P., Parés, J.M., Schleicher, A.M., Pueyo-Anchuela, O., 2009. Complex magnetic subfabrics in a well-developed cleavage domain, Internal Sierras (Pyrenees, Spain). *J. Struct. Geol.* 31, 163–176.
- Oliva-Urcia, B., Casas, A.M., Soto, R., Villalán, J.J., Kodama, K., 2011. A transtensional basin model for the Argamá basin (central southern Pyrenees) based on magnetic fabric and brittle structures. *Geophys. J. Int.* 184 (1), 111–130.
- Ort, M.H., Newkirk, T.T., Vilas, J.F., Vazquez, J.A., 2015. Towards the definition of AMS facies in the deposits of pyroclastic density currents. *Geol. Soc. Lond., Spec. Publ.* 396 (1), 205–226.
- Padovano, M., Elter, F.M., Pandeli, E., Franceschelli, M., 2011. The East Variscan Shear Zone: new insights into its role in the Late Carboniferous collision in southern Europe. *Int. Geol. Rev.* 54 (8), 957–970. <https://doi.org/10.1080/00206814.2011.626120>.
- Padovano, M., Dorr, W., Elter, F.M., Gerdes, A., 2014. The East Variscan Shear Zone: Geochronological constraints from the Capo Ferro area (NE Sardinia, Italy). *Lithos* 196–197, 27–41. <https://doi.org/10.1016/j.lithos.2014.01.015>.
- Paquereau-Lebti, P., Fornari, M., Roperch, P., Thouret, J.C., Macedo, O., 2008. Paleomagnetism, magnetic fabric, and ⁴⁰Ar/³⁹Ar dating of Pliocene and Quaternary ignimbrites in the Arequipa area, southern Peru. *Bull. Volcanol.* 70 (8), 977–997.
- Parés, J.M., Van der Pluijm, B.A., 2002. Phyllosilicate fabric characterization by Low-temperature anisotropy of magnetic susceptibility (LT-AMS). *Geophys. Res. Lett.* 29 (24).
- Pastor-Galán, D., Gutiérrez-Alonso, G., Zulauf, G., Zanella, F., 2012. Analogue modeling of lithospheric-scale oroclinal buckling: constraints on the evolution of the Iberian-Armorican Arc. *Bulletin* 124 (7–8), 1293–1309.
- Pastor-Galán, D., Groenewegen, T., Brouwer, D., Krijgsman, W., Dekkers, M.J., 2015. One or two oroclines in the Variscan orogen of Iberia? Implications for Pangea amalgamation. *Geology* 43 (6), 527–530.
- Pereira, M.F., Gama, C., 2017. Detrital provenance of the Upper Triassic siliciclastic rocks from Southwest Iberia: a review. *J. Iber. Geol.* 43 (3), 379–393.
- Pereira, M.F., Silva, J.B., Drost, K., Chichorro, M., Apraiz, A., 2010. Relative timing of transcurrent displacements in northern Gondwana: U–Pb laser ablation ICP-MS zircon and monazite geochronology of gneisses and sheared granites from the western Iberian Massif (Portugal). *Gondwana Res.* 17 (2–3), 461–481.
- Pereira, M.F., Castro, A., Chichorro, M., Fernández, C., Diaz-Alvarado, J., Martí, J., Rodríguez, C., 2014. Chronological link between deep-seated processes in magma chambers and eruptions: Permo-Carboniferous magmatism in the core of Pangaea (Southern Pyrenees). *Gondwana Res.* 25 (1), 290–308.
- Pereira, M.F., Castro, A., Fernández, C., 2015. The inception of a Paleotethyan magmatic arc in Iberia. *Geosci. Front.* 6 (2), 297–306.
- Pereira, M.F., Gama, C., Rodríguez, C., 2017. Coeval interaction between magmas of contrasting composition (Late Carboniferous–Early Permian Santa Eulália-Monforte massif, Ossa-Morena Zone): field relationships and geochronological constraints. *Geol. Acta* 15 (4), 0409–0428.
- Phillips, F.C., 1977. *La Aplicación de la Proyección Estereográfica en Geología Estructural*. H. Blume Ediciones, Madrid, p. 132.
- Pioli, L., Lanza, R., Ort, M., Rosi, M., 2008. Magnetic fabric, welding texture and strain fabric in the Nuraxi Tuff, Sardinia, Italy. *Bull. Volcanol.* 70 (9), 1123–1137.
- Porreca, M., Mattei, M., Giordano, G., De Rita, D., Funiello, R., 2003. Magnetic fabric and implications for pyroclastic flow and lahar emplacement, Albano maar, Italy. *J. Geophys. Res. Solid Earth* 108 (B5).
- Pueyo, E.L., Román-Berdiel, M.T., Bouchez, J.L., Casas, A.M., Larrasoña, J.C., 2004. Statistical significance of magnetic fabric data in studies of paramagnetic granites. *Geol. Soc. Lond., Spec. Publ.* 238 (1), 395–420.
- Román-Berdiel, T., Casas, A.M., Oliva-Urcia, B., Pueyo, E.L., Rillo, C., 2004. The main Variscan deformation event in the Pyrenees: new data from the structural study of the Bielsa granite. *J. Struct. Geol.* 26 (4), 659–677.
- Saura, E., 2004. *Anàlisi Estructural de la Zona de les Nogueres Pirineus Centrals*. PhD Thesis Universitat Autònoma de Barcelona 92 p.
- Saura, E., Teixell, A., 2006. Inversion of small basins: effects on structural variations at the leading edge of the Axial Zone antiformal stack (Southern Pyrenees, Spain). *J. Struct. Geol.* 28 (11), 1909–1920.
- Schmincke, H.U., 1967. Flow directions in Columbia River Basalt flows and paleocurrents of interbedded sedimentary rocks, south-Central Washington. *Geol. Rundsch.* 56 (1), 992–1020.
- Schneider, C.A., Rasband, W.S., Eliceiri, K.W., 2012. NIH Image to ImageJ: 25 years of image analysis. *Nat. Methods* 9, 671–675.
- Smith, J.V., 2002. Structural analysis of flow-related textures in lavas. *Earth Sci. Rev.* 57 (3–4), 279–297.
- Soriano, C., Beaud, E., Garcés, M., 2008. Magma flow in dikes from rift zones of the basaltic shield of Tenerife, Canary Islands: implications for the emplacement of buoyant magma. *J. Volcanol. Geotherm. Res.* 173 (1–2), 55–68.
- Speksnijder, A., 1985. Anatomy of a strike-slip fault controlled sedimentary basin, Permian of southern Pyrenees, Spain. *Sediment. Geol.* 44, 179–223.
- Tarling, D., Hrouda, F. (Eds.), 1993. *Magnetic Anisotropy of Rocks*. Chapman and Hall, London, p. 214.
- Toprak, V., 1998. Vent distribution and its relation to regional tectonics, Cappadocian Volcanics, Turkey. *J. Volcanol. Geotherm. Res.* 85 (1–4), 55–67.
- Toramaru, A., 1988. Formation of propagation pattern in two-phase flow systems with application to volcanic eruptions. *Geophys. J. Int.* 95 (3), 613–623.
- Tripanera, D., Porreca, M., Urbani, S., Kissel, C., Winkler, A., Sagnotti, L., Nazzareni, V., Acocella, V., 2020. Interpreting inverse magnetic fabric in Miocene dikes from Eastern Iceland. *J. Geophys. Res. Solid Earth* 125 (11). <https://doi.org/10.1029/2020JB020306>.
- Urrutia-Fucugauchi, J., Radakrishnamurthy, C., Negendank, J.F.W., 1984. Magnetic properties of a columnar basalt from Central Mexico. *Geophys. Res. Lett.* 11 (9), 832–835.
- Valero-Garcés, B.L., 1990. *Los Sistemas Lacustres Carbonatados del Stephaniense y Pérmico en el Pirineo Central y Oriental*. (Doctoral dissertation, PhD Thesis University of Zaragoza 413 p).
- Van Den Driessche, J., Brun, J.P., 1989. Un modèle cinématique de l'extension paléozoïque supérieur dans le Sud du Massif Central. *Comptes Rendus de l'Académie des Sciences. Série 2, Mécanique, Physique, Chimie, Sciences de l'univers, Sciences de la Terre* 309 (16), 1607–1613.
- Van der Voo, R., 1969. Paleomagnetic evidence for the rotation of the Iberian Peninsula. *Tectonophysics* 7 (1), 5–56.
- Waters, A.C., 1960. Determining direction of flow in basalts. *Am. J. Sci.* 258, 350–366.
- Weil, A.B., Van der Voo, R., 2002. Insights into the mechanism for orogen-related carbonate remagnetization from growth of authigenic Fe-oxide: a scanning electron microscopy and rock magnetic study of Devonian carbonates from northern Spain. *J. Geophys. Res. Solid Earth* 107 (B4), EPM-1.
- White, J.D.L., Houghton, B.F., 2006. Primary volcanoclastic rocks. *Geology* 34 (8), 677–680.